Astrophysics and Space Science
DOI 10.1007/s•••••-•••-••••-•

Oxygen abundance in local disk and bulge: chemical evolution with a strictly universal IMF

R. Caimmi, E. Milanese
Astronomy Department, Padua University, Vicolo Osservatorio 2, 35122 PADOVA (Italy)

arXiv:0810.0892v2 [astro-ph] 4 Jun 2009

© Springer-Verlag ••••

Abstract This paper has two parts: one about observational constraints related to the empirical differential oxygen abundance distribution (EDOD), and the other about inhomogeneous models of chemical evolution, in particular the theoretical differential oxygen abundance distribution (TDOD). In the first part, the EDOD is deduced from subsamples related to two different samples involving (i) $N = 532$ solar neighbourhood (SN) stars within the range, $-1.5 <$[Fe/H]< 0.5, for which the oxygen abundance has been determined both in presence and in absence of the local thermodynamical equilibrium (LTE) approximation [Ramirez et al., Astron. Astrophys. **4**65, 271 (2007)]; and (ii) $N = 64$ SN thick disk, SN thin disk, and bulge K-giant stars within the range, $-1.7 <$[Fe/H]< 0.5, for which the oxygen abundance has been determined [Melendez et al., Astron. Astrophys. **4**84, L21 (2008)]. A comparison is made with previous results implying use of [O/H]-[Fe/H] empirical relations [Caimmi, Astron. Nachr. **3**22, 241 (2001b); Caimmi, New Astron. **1**2, 289 (2007)] related to (iii) 372 SN halo subdwarfs [Ryan and Norris, Astron. J. **101**, 1865 (1991)]; and (iv) 268 K-giant bulge stars [Sadler et al., Astron. J. **1**12, 171 (1996)]. The EDOD of the SN thick + thin disk is determined by weighting the mass, for assumed SN thick to thin disk mass ratio within the range, 0.1-0.9.

In the second part, inhomogeneous models of chemical evolution for the SN thick disk, the SN thin disk, the SN thick + thin disk, the SN halo, and the bulge, are computed assuming the instantaneous recycling approximation. The EDOD data are fitted, to an acceptable extent, by their TDOD counterparts with the exception of the thin or thick + thin disk, where two additional restrictions are needed: (i) still undetected, low-oxygen abundance thin disk stars exist, and (ii) a single oxygen overabundant star is removed from a thin disk subsample. In any case, the (assumed power-law) stellar initial mass function (IMF) is universal but gas can be inhibited from, or enhanced in, forming stars at different rates with respect to a selected reference case. Models involving a strictly universal IMF (i.e. gas neither inhibited from, nor enhanced in, forming stars with respect to a selected reference case) can also reproduce the data to an acceptable extent.

Our main conclusions are (1) different models are necessary to fit the (incomplete) halo sample, which is consistent with the idea of two distinct halo components: an inner, flattened halo in slow prograde rotation, and an outer, spherical halo in net retrograde rotation [Carollo et al., Nature **4**50, 1020 (2007)]; (2) the oxygen enrichment within the inner SN halo, the SN thick disk, and the bulge, was similar and coeval within the same metallicity range, as inferred from observations [Prochaska et al., Astron. J. **1**20, 2513 (2000)]; (3) the fit to thin disk data implies an oxygen abundance range similar to its thick disk counterpart, with the extension of conclusion (2) to the thin disk, and the evolution of the thick + thin disk as a whole [Haywood, Mon. Not. R. Astron. Soc. **3**88, 1175 (2008)] cannot be excluded; (4) leaving outside the outer halo, a fit to the data related to different environments is provided by models with a strictly universal IMF but different probabilities of a region being active, which implies different global efficiencies of the star formation rate; (5) a special case of stellar migration across the disk can be described by models with enhanced star formation, where a fraction of currently observed SN stars were born *in situ* and a comparable fraction is due to the net effect of stellar migration, according to recent results based on high-resolution N-body + smooth particle hydrodynamics simulations [Roškar et al., Astrophys. J. Lett. **6**84, L79 (2008)].

Keywords galaxies: evolution - stars: formation; evolution.

R. Caimmi, E. Milanese

1 Introduction

The synthesis of α-elements (such as O, Ne, Mg, Si, S, Ca) takes place within SnII progenitors, via reactions of the type, E + $\alpha \rightarrow$ E$'$ + γ, where E, E$'$, are generic elements (E lighter than E$'$), α is a helium nucleus, and γ a photon. Accordingly, α-elements are primary elements, for which the yield is not sensitive to the initial abundance of carbon or other heavy elements in the progenitor, because they are synthesized directly from hydrogen and helium. The abundances of α-elements as a function of the metal content provide crucial information about the stellar initial mass function (IMF) and formation history (e.g., Tinsley (1980); Pagel (1989); Prochaska et al. (2000); Ramirez et al. (2007); Melendez et al. (2008)), and make a main constraint on models of chemical evolution. Among α-elements, oxygen has a special role, in that it is the most abundant element in the universe, after hydrogen and helium.

Unfortunately, oxygen is more difficult than iron (which is not an α-element) to detect, and empirical relations were used to express the former as a function of the latter (e.g., Barbuy (1988); Pagel (1989); Abia and Rebolo (1989); Carretta et al. (2000); Gratton et al. (2000); Takada-Hidai et al. (2001); Israelian et al. (2001); for a review refer to Barbuy et al. (2001)). Only recently, direct oxygen abundance determinations on solar neighbourhood (SN) thick disk, thin disk, and halo stars[1], and bulge stars have been performed (e.g., Ramirez et al. (2007); Melendez et al. (2008)). Different oxygen abundance at any given iron abundance range in common between two selected environments implies related stars were formed from different mixtures of gas, presumably at different epochs and/or locations. Oxygen abundance patterns and their systematic diversities between environment stars thus constrain important information about the assembling and evolution of the Galaxy.

In particular, the chemical abundance of thick disk stars suggests a similar history to those of metal-rich ([Fe/H]$\approx$ -1.3) halo stars, and the thick disk abundance patterns show excellent agreement with the chemical abundances observed in metal-poor ([Fe/H]$\lesssim$ -0.4) bulge stars, suggesting the two populations were formed from the same reservoir at a common epoch, regardless of the exact physical process involved in their formation (Prochaska et al. (2000)). Additional support to the last conclusion is provided by recent findings (Melendez et al. (2008)). On the other hand, a different dynamical signature is exhibited by the Galactic spheroid and disk, which makes evidence for a distinct halo-bulge and thick disk - thin disk collapse, as shown by different empirical distributions of specific angular momentum (Wyse and Gilmore (1992); Ibata and Gilmore (1995)).

Concerning metal abundance distributions in SN disk stars, it has been recognized that earlier results based on spectral type selection, were biased against stars with solar metallicity or higher, with respect to recent results based on colour selection (Haywood (2001, 2006). Oxygen abundance distributions in SN disk stars, or thick disk and thin disk separately, can be deduced from recent direct determinations (Ramirez et al. (2007)). The same cannot be done for halo and bulge stars, with the exception of restricted samples (e.g., Ramirez et al. (2007); Melendez et al. (2008)), and some empirical [O/H]-[Fe/H] relation must be used (e.g., Caimmi (2007), hereafter quoted as C07). Recent analysis on high-resolution infrared spectra of giant stars, show no chemical distinction between the bulge and the SN thick disk (Melendez et al. (2008)).

Inhomogeneous (i.e. implying inhomogeneous star formation) models of chemical evolution succeed in both providing a solution to the G-dwarf problem and reproducing substantial scatter exhibited by the empirical SN age-metallicity relation (e.g., Malinie et al. (1993); Caimmi (2000), Caimmi (2001a), hereafter quoted together as C00; Caimmi (2001b), hereafter quoted as C01; C07; Caimmi (2008), hereafter quoted as C08). The current paper aims to investigate if inhomogeneous simple models of chemical evolution with strictly universal IMF (implying gas is neither inhibited from, nor enhanced in, forming stars with regard to different environments) provide an acceptable fit to the oxygen abundance distribution in the SN thick disk, SN thin disk, SN halo, and bulge, for which new data are available, even if biased towards low metallicities or incomplete. Though the existence of a universal IMF has recently been questioned (e.g., Ballero et al. (2007a)), it appears as a natural consequence of similar (but not necessarily shared) chemical evolution histories experienced by the metal-rich SN halo and the SN thick disk on one hand (Prochaska et al. (2000)), and the bulge and the SN thick disk on the other hand (Melendez et al. (2008)).

The oxygen abundance is deduced from a sample ($N = 523$) of SN disk and SN halo stars (Ramirez et al. (2007)), hereafter quoted as the Ra07 sample, from which four subsamples are extracted following the prescriptions of the authors, related to thick disk ($N = 133$), thin disk ($N = 310$), halo ($N = 28$), and uncertain population ($N = 51$) stars, hereafter quoted as the RaK07, RaN07, RaH07, and RaU07 subsample, respectively. The RaK07 subsample is biased against low ([Fe/H]$\lesssim -1$) metallicities, and the RaH07 subsample is incomplete (Ramirez et al. (2007)). For the bulge and the halo earlier results (C07) are also used, where oxygen abundance is deduced from iron abundance using empirical relations, with regard to a sample ($N = 268$) of bulge K giants in Baade′s window (Sadler et al. (1996)), hereafter quoted as the Sa96 sample, and a sample ($N = 372$) of kinematically selected halo subdwarfs (Ryan and Norris (1991)), hereafter quoted as the RN91 sample.

---

[1] In general, SN stars are to be intended as "passing through the solar neighbourhood" (e.g., Ryan and Norris (1991)).

The oxygen abundance is also deduced from a more restricted sample ($N = 68$) of SN disk, SN halo, and bulge stars (Melendez et al. (2008)), hereafter quoted as the Ma08 sample, which is subdivided into four subsamples, related to the thick disk ($N = 21$), thin disk ($N = 24$), halo ($N = 4$), and bulge ($N = 19$), hereafter quoted as the MaK08, MaN08, MaH08, and MaB08 subsample, respectively. All objects have similar stellar parameters but cover a broad range in metallicity. Oxygen and iron abundances were determined from a standard one-dimension (1D) local thermodynamic equilibrium analysis. Systematic errors were minimized using a homogeneous and differential analysis of the bulge, halo, thick disk, and thin disk stars. For further details refer to the parent paper (Melendez et al. (2008)).

The value of solar oxygen abundance also affects the [O/Fe]-[Fe/H] relation. Recent determinations point towards lower values (e.g., Allende-Prieto et al. (2001); Sofia and Meyer (2001); Asplund et al. (2004); Melendez (2004)), but the question is still under debate (e.g., Landi et al. (2007); Socas-Navarro and Norton (2007)); Centeno and Socas-Navarro (2008); Caffau et al. (2008)). A solar oxygen mass abundance, $(Z_{\mathrm{O}})_\odot = 0.0056$, deduced from Allende-Prieto et al. (2001), shall be used to preserve comparison with earlier results (C01, C07, C08).

Due to the above mentioned uncertainties, it has been preferred to deal with less recent iron abundance determinations to preserve comparison with earlier work (C01, C07, C08), where direct oxygen abundance determinations are still lacking. More recent, statistically more significant and less well scrutinised determinations e.g., the Geneva-Copenhagen survey (Nordström et al. (2004)) for the SN disk and the Hamburg/ESO survey (Schörck et al. (2008)) for the metal-poor SN halo, are related to iron abundance instead of oxygen abundance as in e.g., Ra07 and Ma08 samples, and for this reason shall not be used in the current attempt.

The empirical, differential, oxygen abundance distribution (EDOD), $\psi = \Delta N/\ (N\Delta\phi)$, $\log\phi =$[O/H], is determined in Section 2 for RaK07, RaN07, RaH07, RaU07, and MaK08, MaN08, MaB08, subsamples. In addition, a putative EDOD is derived for the SN thick + thin disk by weighting the mass of the related subsystems, in Section 3. A comparison with the predictions of simple inhomogeneous models, is given in Section 4. The discussion and related implications for the formation of the Galaxy are the subject of Section 5. Some concluding remarks are reported in Section 6.

2 The data

2.1 The empirical differential oxygen abundance distribution

While observations are related to logarithmic number abundances, [E/H]=log(E/H) − log($\mathrm{E}_\odot/\mathrm{H}_\odot$), models of chemical evolution deal with mass abundances, $Z_{\mathrm{E}} = M_{\mathrm{E}}/M$, where E is a generic element heavier than He, M_{E} and M are the total mass under the form of the element, E, and of all elements, respectively. The following relation (Pagel (1989); Malinie et al. (1993); Rocha-Pinto and Maciel (1996); C00, C01, C07, C08):

$$\log\phi = \log\frac{Z_{\mathrm{O}}}{(Z_{\mathrm{O}})_\odot} = \left[\frac{\mathrm{O}}{\mathrm{H}}\right] \quad ; \qquad (1)$$

holds to a good extent. For a formal derivation refer to earlier work (C07, Appendix A).

Following previous attempts (Pagel (1989); Malinie et al. (1993); Rocha-Pinto and Maciel (1996)), the comparison between model predictions and observations shall be performed using the differential instead of the cumulative metallicity distribution, as it is a more sensitive test (Pagel (1989)) and allows direct comparison between different samples (Rocha-Pinto and Maciel (1996)). The occurrence of a sensitivity error in performing observations, precludes the use of a proper differential notation in dealing with the EDOD. This is the reason why the bin length cannot be lower than the sensitivity error, and differential ratios i.e. first derivatives, $\mathrm{d}N/\,\mathrm{d}\phi$, must be replaced by increment ratios, $\Delta N/\Delta\phi$, where $\Delta\phi$ is the bin length, ΔN the number of sample objects within the selected bin, and N is the total number of sample objects.

Accordingly, the EDOD in a selected class of objects is defined as:

$$\psi(\phi \mp \Delta^{\mp}\phi) = \log\frac{\Delta N}{N\Delta\phi} \quad ; \qquad (2a)$$

$$\phi = \frac{\phi^+ + \phi^-}{2} \quad ; \qquad \Delta^{\mp}\phi = \frac{\phi^+ - \phi^-}{2} \quad ; \qquad (2b)$$

$$\phi^{\mp} = \exp_{10}\,[\mathrm{O/H}]^{\mp} \quad ; \qquad (2c)$$

where in general, $\exp_\xi$ defines the power of basis, ξ (in particular, exp defines the power of basis, e, according to the standard notation), and the increment ratio, $\Delta N/\Delta\phi$, used in earlier attempts (Pagel (1989); Malinie et al. (1993)) has been replaced by its normalized counterpart, $\Delta N/\ (N\Delta\phi)$, used in more recent investigations (Rocha-Pinto and Maciel (1996); C00, C01, C07, C08), to allow comparison between different samples. The uncertainty on ΔN has been evaluated from Poisson errors (e.g., Ryan and Norris (1991)), as $\sigma_{\Delta N} = (\Delta N)^{1/2}$, and the related uncertainty in the EDOD is (e.g., C01, C07, C08):

$$\Delta^{\mp}\psi = |\psi - \psi^{\mp}| = \log\left[1 \mp \frac{(\Delta N)^{1/2}}{\Delta N}\right] \quad ; \tag{3a}$$

$$\psi^{\mp} = \log\frac{\Delta N \mp (\Delta N)^{1/2}}{N\Delta\phi} \quad ; \tag{3b}$$

where $\psi^- \to -\infty$ in the limit $\Delta N \to 1$. For further details refer to earlier work (C01).

In the following tables and figures, the bin sizes in normalized oxygen abundance, ϕ, shall correspond to uniform bin sizes in [O/H] (or [Fe/H] if an empirical [O/H]-[Fe/H] relation is used), which implies non uniform bin sizes, $\Delta\phi = 2\Delta^{\mp}\phi$, as shown in Table 1.

2.2 Oxygen abundance distribution in subsamples

The Ra07 sample is considered, where oxygen abundance is directly inferred both in presence and in absence of the local thermodynamic equilibrium (LTE) approximation (Ramirez et al. (2007), Table 6, available at the CDS). The LTE approximation well holds deep in the stellar photosphere, and a continuous transition occurs up to complete non-equilibrum (NLTE) high in the atmosphere. For further details refer to specialized textbooks (e.g., Gray (2005), Chapter 6).

The metallicity range is $-1.5 \le$ [Fe/H] ≤ 0.5, but the sample is biased against lower metallicities, [Fe/H]$\lesssim -1$. On the other hand, it is expected to be unbiased at higher metallicities, for the following reasons: (i) more than 90% of the sample stars are located within 100 pc from the sun, and (ii) the related differential iron abundance distribution looks similar to its counterpart deduced from different SN disk samples (Wyse and Gilmore (1995); Jørgensen (2000); Haywood (2001); Fuhrmann (2008)), and the same holds for SN thick disk and thin disk subsamples, when comparison may be performed. The EDOD has been deduced from the Ra07 sample in an earlier attempt (C08), both in presence and in absence of LTE approximation.

Under the assumption that sample objects belong to three stellar populations (thick disk, thin disk, halo), each with a Gaussian velocity distribution, the probability of a star being located in one of the components, may be expressed as a function of the Galactic space velocities, $P_i = P_i(U, V, W)$, where $i = 1, 2, 3$, for the thin disk, the thick disk, and the halo, respectively; a $P_i > 0.7$ constraint is set to determine the membership of sample objects to the i population (Ramirez et al. (2007)).

Using the above mentioned prescriptions, the Ra07 sample has been subdivided into four subsamples: RaN07, RaK07, RaH07, RaU07, where $P_1 > 0.7$, $P_2 > 0.7$, $P_3 > 0.7$, $P_i \le 0.7$, $i = 1, 2, 3$, respectively. The RaH07 subsample is by far incomplete, as [Fe/H]> -1.5 for sample objects and any attempt to trace a halo abundance trend using only the metal-rich tail is dubious (Ramirez et al., 2007). With this caveat in mind, the RaH07 subsample shall be considered together with the RaU07 subsample.

On the other hand, it can be seen (Ramirez et al. (2007)) that a similar [O/Fe]-[Fe/H] empirical relation is exhibited by RaK07 and RaH07 subsamples:

$$[\mathrm{O/Fe}] = a_\mathrm{O} + b_\mathrm{O}[\mathrm{Fe/H}] \quad ; \tag{4}$$

where $a_\mathrm{O} = 0.370 \mp 0.027$, $b_\mathrm{O} = -0.121 \mp 0.043$, $N_\mathrm{O} = 43$, $\sigma_\mathrm{O} = 0.065$, for the RaK07 subsample; $a_\mathrm{O} = 0.388 \mp 0.049$, $b_\mathrm{O} = -0.048 \mp 0.071$, $N_\mathrm{O} = 12$, $\sigma_\mathrm{O} = 0.072$, for the RaH07 subsample; in addition, N_O is the number of stars used for the fit and σ_O the random scatter around the mean fit.

The Ma08 sample is also considered, where oxygen abundance is deduced from a standard 1D local thermodynamic equilibrium analysis, and systematic errors are minimized using a homogeneous and differential analysis of stars belonging to different populations (Melendez et al. (2008)). The Ma08 sample is made of four subsamples: MaK08, MaN08, MaH08, MaB08, within the metallicity range, $-1.7 \le$ [Fe/H] ≤ 0.5.

A similar fit, expressed by Eq. (4), is shown using MaB08 and MaK08 subsamples, where $a_\mathrm{O} = 0.41$, $b_\mathrm{O} = -0.02$, $N_\mathrm{O} = 19$, $\sigma_\mathrm{O} = 0.09$, for the MaB08 subsample, and $a_\mathrm{O} = 0.39$, $b_\mathrm{O} = -0.01$, $N_\mathrm{O} = 21$, $\sigma_\mathrm{O} = 0.09$, for the MaK08 subsample (Melendez et al. (2008)). It can also be seen that oxygen abundance patterns exhibited by the MaH08 subsample are very close to their counterparts related to the MaB08 and MaK08 subsamples (Melendez et al. (2008), Fig. 2).

In conclusion, a similar trend for the [O/Fe]-[Fe/H] relation with respect to the SN thick disk, the bulge, and the SN halo, is deduced from both Ra07 and Ma08 samples, in the metallicity range where the thick disk is unambiguously defined.

2.3 Oxygen abundance distribution in SN thick disk

Both RaK07 and MaK08 subsamples are considered to infer separate EDODs related to the SN thick disk, for comparison with model predictions. The oxygen abundance range is $-0.60 < \mathrm{[O/H]} < 0.45$ (LTE), $-0.80 \le \mathrm{[O/H]} < 0.45$ (NLTE), for the RaK07 subsample, and $-1.40 < \mathrm{[O/H]} < 0.30$ for the MaK08 subsample.

The EDOD related to the RaK07 subsample is listed in Table 2 and plotted in Fig. 1, upper (LTE) and lower (NLTE) left, where the dashed vertical bands correspond to $\mathrm{[Fe/H]} = -1$ and related uncertainty, deduced from Eq. (4) in dealing with the thick disk (Ramirez et al. (2007)).

The EDOD related to the MaK08 subsample is listed in Table 3 (left) and plotted in Fig. 2 (upper left).

It can be seen that EDODs deduced from RaK07 and MaK08 subsamples show qualitative agreement, leaving aside the low-metallicity ($\mathrm{[Fe/H]} < -1$) tail where, on the other hand, oxygen abundance bins are poorly populated and the statistical relevance is weak.

2.4 Oxygen abundance distribution in SN thin disk

Both RaN07 and MaN08 subsamples are considered to infer separate EDODs related to the SN thin disk, for comparison with model predictions. The oxygen abundance range is $-0.35 < \mathrm{[O/H]} < 0.60$ (LTE), $-0.45 < \mathrm{[O/H]} < 0.45$ (NLTE), for the RaN07 subsample, and $-1.00 < \mathrm{[O/H]} < 0.30$ for the MaN08 subsample.

The EDOD related to the RaN07 subsample is listed in Table 4 and plotted in Fig. 1, upper (LTE) and lower (NLTE) right, where the dashed vertical bands correspond to $\mathrm{[Fe/H]} = -1$ and related uncertainty, deduced from Eq. (4) in dealing with the SN thin disk (Ramirez et al. (2007)).

The EDOD related to the MaN08 subsample is listed in Table 3 (right) and plotted in Fig. 2 (upper right).

It can be seen that EDODs deduced from RaN07 and MaN08 subsamples show qualitative agreement, leaving aside the low-metallicity ($\mathrm{[Fe/H]} < -1$) tail where, on the other hand, oxygen abundance bins are poorly populated and the statistical relevance is weak.

2.5 Oxygen abundance distribution in the bulge

The MaB08 subsample is considered to infer the EDOD related to the bulge, for comparison with model predictions. The oxygen abundance range is $-1.3 < \mathrm{[O/H]} < 0.5$.

The EDOD related to the MaB08 subsample is listed in Table 5 and plotted in Fig. 2 (lower right).

Table 1 Logarithmic and numerical bins in oxygen abundance. Upper and lower values for each bin are denoted as $\mathrm{[O/H]}^{\mp} = \log \phi^{\mp}$, according to Eqs. (1) and (2b). Logarithmic bins which differ by 1 dex are related to numerical bins which differ by a factor 10, which makes an (up and down) endless recursion of the table

$\mathrm{[O/H]}^{-}$	$\mathrm{[O/H]}^{+}$	ϕ	$\Delta^{\mp}\phi$
0.05	0.15	1.2673 E+0	1.4526 E−1
0.15	0.25	1.5954 E+0	1.8287 E−1
0.25	0.35	2.0085 E+0	2.3022 E−1
0.35	0.45	2.5286 E+0	2.8983 E−1
0.45	0.55	3.1833 E+0	3.6488 E−1
0.55	0.65	4.0075 E+0	4.5935 E−1
0.65	0.75	5.0451 E+0	5.7829 E−1
0.75	0.85	6.3514 E+0	7.2802 E−1
0.85	0.95	9.9960 E+0	9.1653 E−1
0.95	1.05	1.0066 E+1	1.1538 E−0
1.05	1.15	1.2673 E+1	1.4526 E−0

Table 5 The empirical, differential oxygen abundance distribution (EDOD) in the bulge, deduced from the MaB08 ($N = 19$) subsample

	BULGE			
ϕ	ψ	$\Delta^{-}\psi$	$\Delta^{+}\psi$	ΔN
5.045 E−2	+6.581 E−1	$+\infty$	3.010 E−1	1
6.351 E−2	+5.581 E−1	$+\infty$	3.010 E−1	1
7.996 E−2				
1.007 E−1				
1.267 E−1				
1.595 E−1				
2.009 E−1	+5.807 E−2	$+\infty$	3.010 E−1	1
2.529 E−1	−4.193 E−2	$+\infty$	3.010 E−1	1
3.183 E−1				
4.008 E−1	−2.419 E−1	$+\infty$	3.010 E−1	1
5.045 E−1	−4.090 E−2	5.333 E−1	2.323 E−1	2
6.351 E−1				
7.996 E−1				
1.007 E−0	−1.648 E−1	3.740 E−1	1.979 E−1	3
1.267 E−0	−4.409 E−1	5.333 E−1	2.323 E−1	2
1.595 E−0	−5.409 E−1	5.333 E−1	2.323 E−1	2
2.009 E−0	−4.648 E−1	3.740 E−1	1.579 E−1	3
2.529 E−0	−1.042 E−0	$+\infty$	3.010 E−1	1
3.183 E−0				
4.008 E−0	−1.242 E−0	$+\infty$	3.010 E−1	1

Table 2 The empirical, differential oxygen abundance distribution (EDOD) in the solar neighbourhood (SN) thick disk, deduced from the RaK07 subsample ($N = 133$) both in presence (LTE) and in absence (NLTE) of the local thermodynamic equilibrium approximation

	LTE				NLTE			
ϕ	ψ	$\Delta^-\psi$	$\Delta^+\psi$	ΔN	ψ	$\Delta^-\psi$	$\Delta^+\psi$	ΔN
1.595 E−1					−6.870 E−1	$+\infty$	3.010 E−1	1
2.009 E−1					−7.870 E−1	$+\infty$	3.010 E−1	1
2.529 E−1	−8.870 E−1	$+\infty$	3.010 E−1	1	−5.860 E−1	5.333 E−1	2.323 E−1	2
3.183 E−1	−6.860 E−1	5.333 E−1	2.323 E−1	2	−6.860 E−1	5.333 E−1	2.323 E−1	2
4.008 E−1	−6.099 E−1	3.740 E−1	1.979 E−1	3	−3.089 E−1	2.279 E−1	1.487 E−1	6
5.045 E−1	−7.099 E−1	3.740 E−1	1.979 E−1	3	−3.419 E−1	2.062 E−1	1.392 E−1	7
6.351 E−1	−4.419 E−1	2.062 E−1	1.392 E−1	7	−3.175 E−2	1.167 E−1	9.191 E−2	18
7.996 E−1	−2.109 E−1	1.297 E−1	9.975 E−2	15	−4.460 E−2	1.041 E−1	8.393 E−2	22
1.007 E−0	+3.149 E−2	8.306 E−2	6.970 E−2	33	−5.566 E−2	9.283 E−2	7.644 E−2	27
1.267 E−0	−1.246 E−1	8.921 E−2	7.397 E−2	29	−2.648 E−1	1.069 E−1	8.572 E−2	21
1.595 E−0	−3.648 E−1	1.069 E−1	8.572 E−2	21	−4.566 E−1	1.206 E−1	9.431 E−2	17
2.009 E−0	−6.731 E−1	1.411 E−1	1.063 E−1	13	−8.833 E−1	1.895 E−1	1.315 E−1	8
2.529 E−0	−1.109 E−0	1.487 E−1	1.487 E−1	6	−1.887 E−0	$+\infty$	3.010 E−1	1

Table 3 The empirical, differential oxygen abundance distribution (EDOD) in the solar neighbourhood (SN) thick disk (left) and SN thin disk (right), deduced from the MaN08 ($N = 24$) and the MaK08 ($N = 21$) subsample, respectively

	THICK DISK				THIN DISK			
ϕ	ψ	$\Delta^-\psi$	$\Delta^+\psi$	ΔN	ψ	$\Delta^-\psi$	$\Delta^+\psi$	ΔN
4.008 E−2	+7.146 E−1	$+\infty$	3.010 E−1	1				
5.045 E−2								
6.351 E−2								
7.996 E−2								
1.007 E−1	+3.146 E−1	$+\infty$	3.010 E−1	1	+2.566 E−1	$+\infty$	3.010 E−1	1
1.267 E−1								
1.595 E−1								
2.009 E−1	+1.461 E−2	$+\infty$	3.010 E−1	1	−4.339 E−2	$+\infty$	3.010 E−1	1
2.529 E−1								
3.183 E−1								
4.008 E−1					−3.4343E−1	$+\infty$	3.010 E−1	1
5.045 E−1					−4.434 E−1	$+\infty$	3.010 E−1	1
6.351 E−1	−1.844 E−1	5.333 E−1	2.323 E−1	2	−6.627 E−2	3.740 E−1	1.979 E−1	3
7.996 E−1	−2.844 E−1	5.333 E−1	2.323 E−1	2	−1.663 E−1	3.740 E−1	1.979 E−1	3
1.007 E−0	+1.597 E−1	2.062 E−1	1.392 E−1	7	−4.442 E−2	2.574 E−1	1.605 E−1	5
1.267 E−0	−1.833 E−1	3.010 E−1	1.761 E−1	4	−1.444 E−1	2.574 E−1	1.605 E−1	5
1.595 E−0	−5.844 E−1	5.333 E−1	2.323 E−1	2	−6.424 E−1	5.333 E−1	2.323 E−1	2
2.009 E−0	−9.854 E−1	$+\infty$	3.010 E−1	1	−7.424 E−1	5.333 E−1	2.323 E−1	2

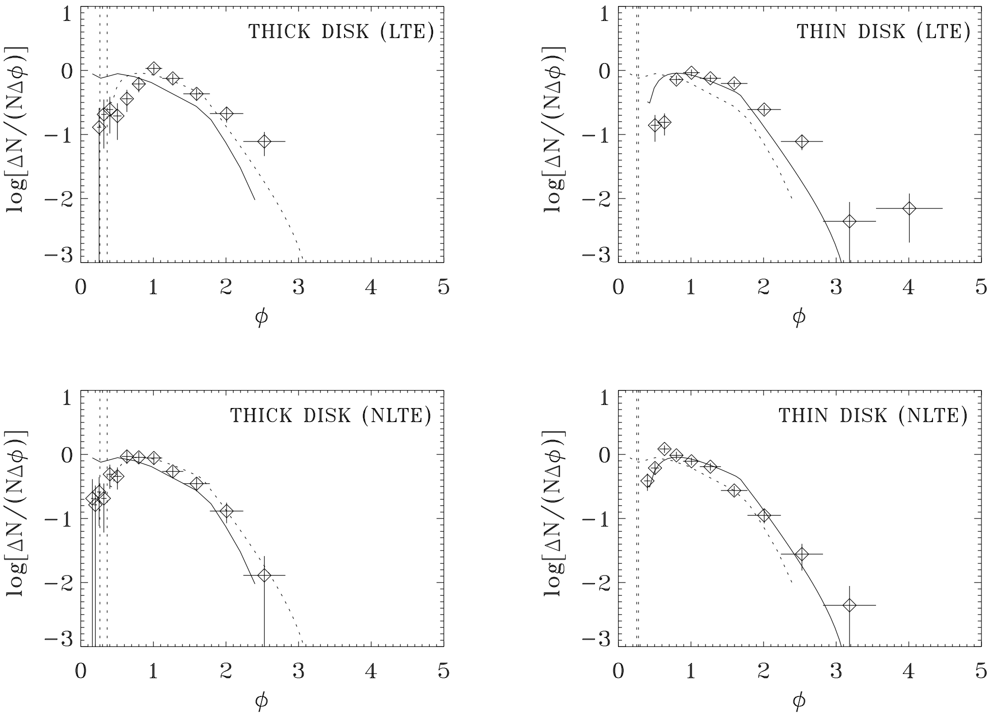

Fig. 1 The empirical, differential oxygen abundance distribution (EDOD) related to the RaK07 (left panels) and RaN07 (right panels) subsample, both in presence (LTE, top panels) and in absence (NLTE, bottom panels) of the local thermodynamic equilibrium approximation. The theoretical, differential oxygen abundance distribution (TDOD) related to inhomogeneous models of chemical evolution for the solar neighbourhood (SN) thick disk (case DB15, left panels) and the SN thin disk (case DN, right panels) are plotted as full curves, and as dotted curves in the remaining panels. Models are fitted to NLTE data. The dashed vertical bands correspond to [Fe/H]$= -1$ and related uncertainties, deduced from Eq. (4) in dealing with the thick (left panels) and the thin (right panels) disk (Ramirez et al. (2007)

It can be seen that EDODs deduced from the MaN08 subsample and the Sa96 sample, where [O/H]-[Fe/H] empirical relations have been used (C07), show qualitative agreement, in spite of the poorly populated oxygen abundance bins, for which the statistical relevance is weak, in the former case.

2.6 Oxygen abundance distribution in the SN halo

The RaH07 subsample is considered to infer the EDOD related to the SN halo only for illustrative purposes, due to its incompleteness. The oxygen abundance range is $-1.00 <$ [O/H] < 0.30 (LTE), $-1.20 <$ [O/H] < 0.20 (NLTE).

The EDOD related to the RaH07 subsample is listed in Table 6 and plotted in Fig. 3 both in presence (upper right) and in absence (lower right) of the LTE approximation.

It can be seen that EDODs deduced from RaH07 and MaB08 subsamples show qualitative agreement.

The EDOD related to the RaU07 subsample is also plotted in Fig. 3 for comparison, both in presence (upper left) and in absence (lower left) of the LTE approximation. The related trend appears to be closer to its SN thick disk and SN thin disk counterparts, with respect to the SN halo.

3 Inferred SN thick + thin disk oxygen abundance distribution

Under the assumption of a universal initial mass function (IMF) for a star generation, the SN thick + thin

Table 4 The empirical, differential oxygen abundance distribution (EDOD) in the solar neighbourhood (SN) thin disk, deduced from the RaN07 subsample ($N = 310$) both in presence (LTE) and in absence (NLTE) of the local thermodynamic equilibrium approximation

	LTE				NLTE			
ϕ	ψ	$\Delta^-\psi$	$\Delta^+\psi$	ΔN	ψ	$\Delta^-\psi$	$\Delta^+\psi$	ΔN
4.008 E−1					−4.131 E−1	1.558 E−1	1.145 E−1	11
5.045 E−1	−8.556 E−1	2.574 E−1	1.605 E−1	5	−2.121 E−1	1.041 E−1	8.393 E−2	22
6.351 E−1	−8.094 E−1	2.062 E−1	1.392 E−1	7	+8.583 E−2	6.290 E−2	5.494 E−2	55
7.996 E−1	−1.418 E−1	7.375 E−2	6.302 E−2	41	−1.417 E−2	6.290 E−2	5.494 E−2	55
1.007 E−0	−3.499 E−2	5.704 E−2	5.042 E−2	66	−1.064 E−1	6.230 E−2	5.447 E−2	56
1.267 E−0	−1.220 E−1	5.614 E−2	4.971 E−2	68	−1.911 E−1	6.113 E−2	5.358 E−2	58
1.595 E−0	−2.033 E−1	5.487 E−2	3.871 E−2	71	−5.632 E−1	8.598 E−2	7.174 E−2	31
2.009 E−0	−6.105 E−1	8.042 E−2	6.783 E−2	35	−9.504 E−1	1.249 E−1	9.691 E−2	16
2.529 E−0	−1.108 E−0	1.351 E−1	1.029 E−1	14	−1.556 E−0	2.574 E−1	1.605 E−1	5
3.183 E−0	−2.355 E−0	+∞	3.010 E−1	1	−2.355 E−0	+∞	3.010 E−1	1
4.008 E−0	−2.154 E−0	5.333 E−1	2.323 E−1	2				

Table 6 The empirical, differential oxygen abundance distribution (EDOD) in the solar neighbourhood (SN) halo, deduced from the RaH07 subsample ($N = 28$) both in presence (LTE) and in absence (NLTE) of the local thermodynamic equilibrium approximation

	LTE				NLTE			
ϕ	ψ	$\Delta^-\psi$	$\Delta^+\psi$	ΔN	ψ	$\Delta^-\psi$	$\Delta^+\psi$	ΔN
6.351 E−2					+3.897 E−1	+∞	3.010 E−1	1
7.996 E−2								
1.007 E−1	−1.897 E−1	+∞	3.010 E−1	1				
1.267 E−1					+8.967 E−2	+∞	3.010 E−1	1
1.595 E−1								
2.009 E−1	−1.103 E−1	+∞	3.010 E−1	1	+4.917 E−1	3.010 E−1	1.761 E−1	4
2.529 E−1	+2.668 E−1	3.740 E−1	1.979 E−1	3				
3.183 E−1	−3.103 E−1	+∞	3.010 E−1	1	+3.886 E−1	2.574 E−1	1.605 E−1	5
4.008 E−1	−1.093 E−1	5.333 E−1	2.323 E−1	2	−1.093 E−1	5.333 E−1	2.323 E−1	2
5.045 E−1	+1.886 E−1	2.574 E−1	1.605 E−1	5	−3.321 E−2	3.740 E−1	1.979 E−1	3
6.351 E−1	−1.332 E−1	3.740 E−1	1.979 E−1	3	−3.093 E−1	5.333 E−1	2.323 E−1	2
7.996 E−1	−2.332 E−1	3.740 E−1	1.979 E−1	3	−1.083 E−1	3.010 E−1	1.761 E−1	4
1.007 E−0	−2.083 E−1	3.010 E−1	1.761 E−1	4	−3.332 E−1	3.740 E−1	1.979 E−1	3
1.267 E−0	−6.093 E−1	5.333 E−1	2.323 E−1	2	−9.103 E−1	+∞	3.010 E−1	1
1.595 E−0	−1.010 E−0	+∞	3.010 E−1	1	−7.093 E−1	5.333 E−1	2.323 E−1	2
2.009 E−0	−8.093 E−1	5.333 E−1	2.323 E−1	2				

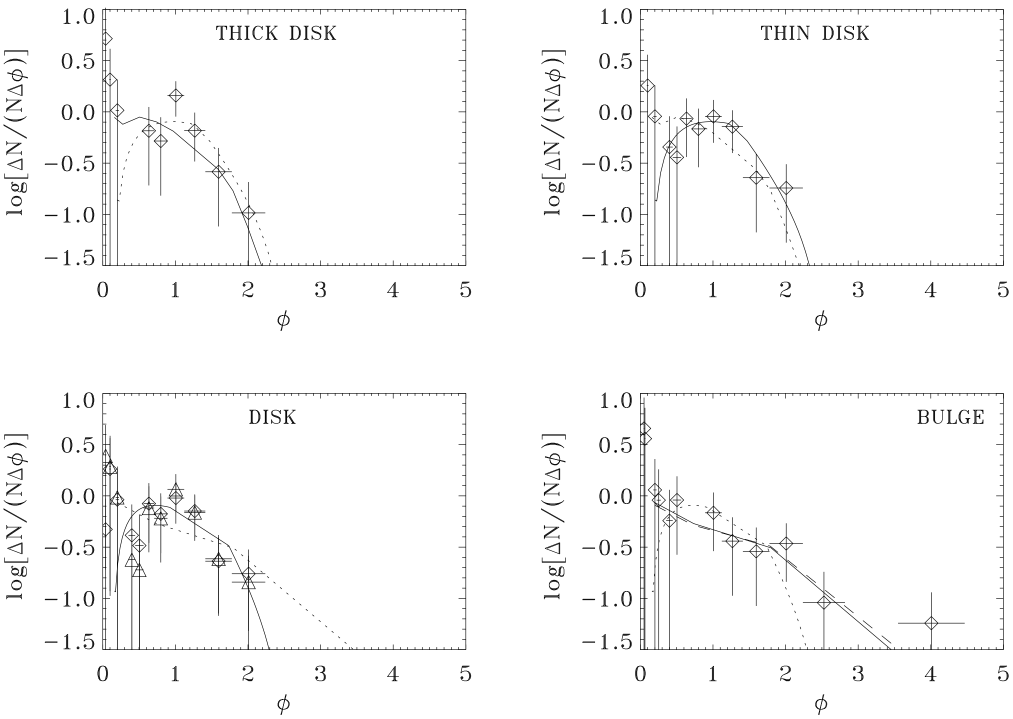

Fig. 2 The empirical, differential oxygen abundance distribution (EDOD) related to the (from top left in clockwise sense) MaK08, MaN08, MaB08, subsample, and a combination of MaK08 and MaN08 subsamples after weighting by mass, for an assumed solar neighbourhood (SN) thick disk to thin disk mass ratio, $M_{\rm KD}/M_{\rm ND} = 0.1$ (diamonds) and 0.9 (triangles). The theoretical, differential oxygen abundance distribution (TDOD) related to inhomogeneous models of chemical evolution for the SN thick disk (case DB15), the SN thin disk (case DN81), the SN thick + thin disk (case KN4), and the bulge (case B) are plotted as full curves. The dotted curve on each panel reproduces (for comparison) the full curve on the other panel of the same row. The dashed curve plotted on the bottom right panel corresponds to a different bulge model (case B1)

disk EDOD may be expressed as (C07, C08):

$$\psi = \log\left[\frac{M_{\rm KD}}{M_{\rm D}}\frac{\Delta N_{\rm KD}}{N_{\rm KD}\Delta\phi} + \frac{M_{\rm ND}}{M_{\rm D}}\frac{\Delta N_{\rm ND}}{N_{\rm ND}\Delta\phi}\right] \quad ; \qquad (5a)$$

$$\Delta^{\mp}\psi = \left|\log\left[1 \mp \frac{\sigma_{\Delta{\rm N/N}}}{\Delta N/N}\right]\right| \quad ; \qquad (5b)$$

$$\psi^{\mp} = \log\left[\frac{M_{\rm KD}}{M_{\rm D}}\frac{\Delta N_{\rm KD} \mp (\Delta N_{\rm KD})^{1/2}}{N_{\rm KD}\Delta\phi} + \frac{M_{\rm ND}}{M_{\rm D}}\frac{\Delta N_{\rm ND} \mp (\Delta N_{\rm ND})^{1/2}}{N_{\rm ND}\Delta\phi}\right] \quad ; \qquad (5c)$$

$$\sigma_{\Delta{\rm N/N}} = \frac{M_{\rm KD}}{M_{\rm D}}\frac{(\Delta N_{\rm KD})^{1/2}}{N_{\rm KD}} + \frac{M_{\rm ND}}{M_{\rm D}}\frac{(\Delta N_{\rm ND})^{1/2}}{N_{\rm ND}} \qquad (5d)$$

where $M_{\rm KD}$ and $M_{\rm ND}$ are the SN thick disk and the SN thin disk mass, $M_{\rm D} = M_{\rm KD} + M_{\rm ND}$, $N_{\rm KD}$ and $N_{\rm ND}$ the number of related sample objects, and $\Delta N_{\rm KD}$, $\Delta N_{\rm ND}$, the number of related sample objects within a selected metallicity bin, Δ[O/H], converted into $\Delta\phi$ using Eq. (2). For further details refer to the parent papers (C07, C08).

In general, the disk is usually conceived as made of two main subsystems: the thick disk and the thin disk. Accordingly, the EDOD related to the SN disk depends, via Eqs. (5), on the SN thick to thin disk mass ratio, $M_{\rm KD}/M_{\rm ND}$, which is poorly known at present. Values already quoted in literature span a wide range, from some percent (e.g., Holmberg et al. (2007)) to about unity (e.g., Fuhrmann (2008)), or even indeterminate in the sense that no distinction can be made (e.g., Norris (1987); Ivezic et al. (2008)). In addition, the global thick to thin disk mass ratio could be different from its SN counterpart, $M_{\rm KD}/M_{\rm ND}$.

The cases, $M_{\rm KD}/M_{\rm ND} = 0.1$, 0.3, 0.5, 0.7, 0.9, deduced from RaK07 and RaN07 subsamples, are represented in Fig. 4 as triangles, diamonds, crosses, squares, asterisks, respectively, both in presence (LTE) and in absence (NLTE) of the LTE approximation. Error bars are plotted in left panels only, to allow comparison.

The cases, $M_{\rm KD}/M_{\rm ND} = 0.1$ and 0.9, deduced from MaK08 and MaN08 subsamples, are represented in Fig. 2 (bottom left) as diamonds and triangles, respectively.

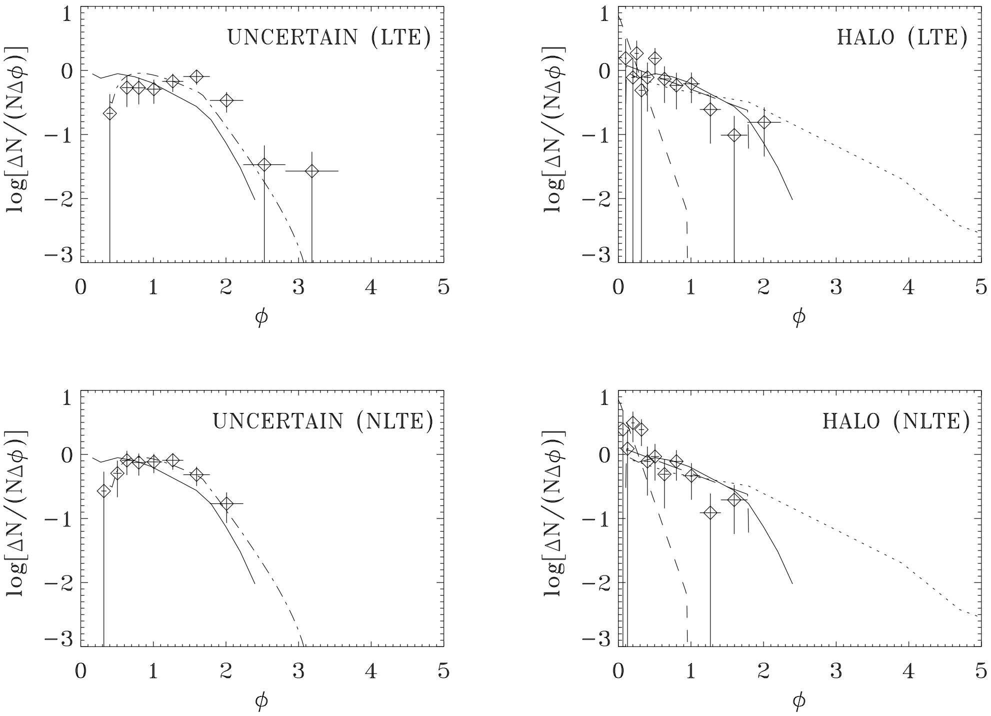

Fig. 3 The empirical, differential oxygen abundance distribution (EDOD) related to the RaU07 (left panels) and RaH07 (right panels) subsample, both in presence (LTE, top panels) and in absence (NLTE, bottom panels) of the local thermodynamic equilibrium approximation. The theoretical, differential oxygen abundance distribution (TDOD) related to inhomogeneous models of chemical evolution for the solar neighbourhood (SN) thick disk (case DB15), the SN thin disk (case DN), and the SN halo (case H) are plotted as full curves, dot-dashed curves, and long-dashed curves, respectively. Models are fitted to NLTE data. Bulge (case B1) and SN halo (case H1) counterparts presented in an earlier attempt (C07) are also shown as dotted and dashed curves, respectively.

An inspection of Figs. 2 (bottom left) and 4 shows that, in both cases, the uncertainty on the thick to thin disk mass ratio is comparable with the error box, except for the low-metallicity tail ([Fe/H]< -1) and/or poorly populated oxygen abundance bins, where a weak statistical relevance is expected.

4 Inhomogeneous, simple models

In the light of inhomogeneous simple models of chemical evolution, a selected system is conceived as being structured into a number of discrete, entirely gaseous, identical regions, and a background of long-lived stars, stellar remnants, and gas inhibited from star formation, which have been generated earlier. The evolution occurs via a sequence of identical time steps. At the beginning of each step, star formation stochastically takes place in a subclass of "active" regions, as described by simple homogeneous models, while the others remain "quiescent". At the end of each step, high-mass stars have died whereas low-mass stars have survived up until today, according to instantaneous recycling approximation. In addition, the enriched gas which remains from active regions is instantaneously mixed with the unenriched gas within quiescent regions, to form a new set of identical regions for the next step. For further details and complete formulation refer to earlier attempts (C01, C07, C08) and parent papers (Malinie et al. (1993); C00). Due to reasons of simplicity, the current investigation shall be restricted to the special case of expected evolution, where the fraction of active regions is time independent. For the general case, refer to earlier attempts (C00, C01).

Input parameters of inhomogeneous models considered in the current attempt and parent papers (C00, C01, C07, C08) are: the number of steps during and after the assembling phase; the IMF power-law exponent; the solar oxygen abundance; the minimum (beginning of the first step) and maximum (end of the last step) normalized oxygen abundance; the maximum normalized oxygen abundance at the end of the first step after the assembling phase; the true and the effective yield; the total number of regions at any step (if taken con-

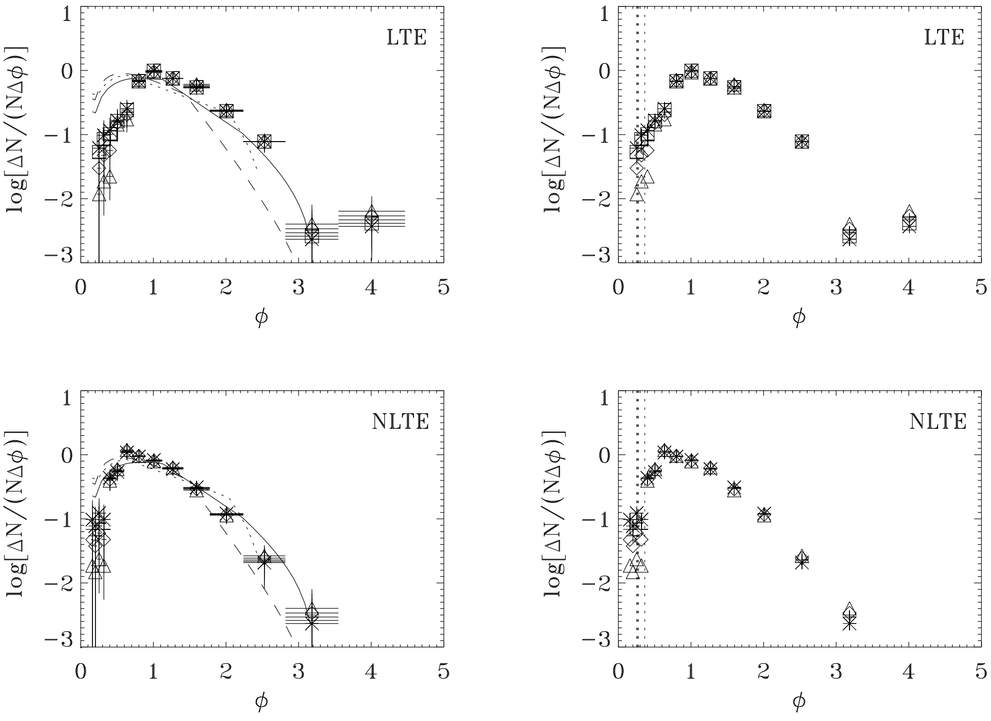

Fig. 4 The empirical, differential oxygen abundance distribution (EDOD) in the solar neighbourhood (SN) thick + thin disk, deduced from RaK07 and RaN07 subsamples, both in presence (LTE, top panels) and in absence (NLTE, bottom panels) of the local thermodynamic equilibrium approximation. Different symbols are related to different thick to thin disk mass ratios, $M_{\mathrm{KD}}/M_{\mathrm{ND}}$. Caption of symbols: $M_{\mathrm{KD}}/M_{\mathrm{ND}} = 0.1$ (triangles); 0.3 (diamonds); 0.5 (crosses); 0.7 (squares); 0.9 (asterisks). Error bars are omitted in right panels to gain clarity. The theoretical, differential oxygen abundance distribution (TDOD) related to inhomogeneous models of chemical evolution for the SN thick + thin disk (cases KN), is plotted as dashed (case KN2) and full (case KN3) curves. Its counterpart, related to the SN thick disk (cases DB), is plotted as dotted (case DB105) curves. The dashed vertical bands on right panels correspond to [Fe/H]= −1 and related uncertainties, deduced from Eq. (4) with regard to a thick disk and a thin disk subsample (Ramirez et al. (2007))

stant during the evolution) or the mass of a region (if taken constant during the evolution); the total number of steps; as shown in Table 7. The more relevant output parameters are listed in Tables 8, 9, and 10. A change in power-law IMF exponent affects only the mass fraction of a star generation, α, which remains locked up in long-lived stars and stellar remnants, and the lower stellar mass limit, m_{mf}, while the remaining parameters are left unchanged. For further details see the parent papers (C01, C07, C08).

Values of input parameters for different models related to the thick disk (models DB), the thin disk (models DN), the thick + thin disk (models KN), the halo (models H), and the bulge (models B) are listed in Table 7. Models B1 and H1 come from earlier work (C07).

Available samples, from which the EDOD has been deduced, are biased (towards low metallicities) and/or incomplete: for this reason, little meaning would be related to the best fit to the data. Different models considered here are mainly aimed in (i) analysing the effect of different input parameters on oxygen enrichment; (ii) providing acceptable fits to the data; (iii) investigating if a class of models with strictly universal IMF exist, which reproduce the EDOD determined for different populations.

An equal number of steps has been chosen for both the assembling phase and the whole evolution, with regard to the halo, the bulge, and the thick disk, which formed within about 1 Gyr (e.g., Prantzos (2008); Zoccali et al. (2008); Melendez et al. (2008)). On the other hand, a larger number of steps has been assumed for the thin disk, which is still undergoing chemical evolution. Accordingly, 4 episodes of star formation (2 during the assembling phase) have been (somewhat arbitrarily) chosen for the halo, the bulge, and the thick disk, and 25 (5 during the assembling phase) for the thin disk.

The initial and final normalized oxygen abundance have been chosen equal to the minimum and maximum value related to the most populated sample. With re-

Table 7 Values of input parameters related to the expected evolution of inhomogeneous simple models, for a number of different cases concerning the thick disk (models DB), the thin disk (models DN), the thick + thin disk (models KN), the halo (models H), and the bulge (models B). The expected evolution is independent of the total number of regions (C00). The assumed solar oxygen abundance is $(Z_{\rm O})_\odot = 0.0056$. The duration of evolution is needed only for specifying the age-metallicity relation (C07, C08). Different values of the IMF power-law exponent, p, leave the output parameters unchanged with the exception of the mass fraction of a star generation, α, which remains locked up in long-lived stars and stellar remnants, and the lower stellar mass limit, $m_{\rm mf}$, as shown in Tables 8, 9, and 10. Symbol captions: $L_{\rm C}$ - number of steps during the assembling phase; $L_{\rm A}$ - number of steps during the whole evolution; $\phi_{\rm min}$ - minimum normalized oxygen abundance; $\phi_{\rm max}$ - maximum normalized oxygen abundance; $\phi^*_{\rm max}$ - maximum normalized oxygen abundance during the $(L_{\rm C}+1)$-th step; a - slope of the empirical differential oxygen abundance distribution of the adjoint simple homogeneous model, see Eq. (6); $\hat{p}$ - true yield; $\hat{p}''$ - effective yield. The high number of digits in $\phi^*_{\rm max}$ is necessary to ensure the same IMF during and after the assembling phase. For further details refer to the parent papers (C00, C01, C07)

case	$L_{\rm C}$	$L_{\rm A}$	$\phi_{\rm min}$	$\phi_{\rm max}$	$\phi^*_{\rm max}$	$-a\hat{p}''/\hat{p}$	$\hat{p}''/\hat{p}$
DB12	2	4	0.160	2.5	2.325653322	0.48	0.40
DB13	2	4	0.160	2.5	2.303503529	0.52	0.40
DB14	2	4	0.160	2.5	2.284610521	0.56	0.40
DB15	2	4	0.160	2.5	2.268320468	0.60	0.40
DN	5	25	0.400	3.2	2.01018844	0.60	0.40
DN4	5	25	0.400	3.2	2.38931821	0.24	0.60
DN5	5	25	0.400	3.2	2.13331046	0.30	0.60
DN6	5	25	0.400	3.2	1.96266176	0.36	0.60
DN7	5	25	0.400	3.2	1.84079119	0.42	0.60
KN1	5	25	0.160	3.2	2.09520539	0.46	0.40
KN2	5	25	0.160	3.2	1.83493684	0.60	0.40
KN3	5	25	0.160	3.2	1.59805348	0.46	0.60
KN4	5	25	0.160	2.5	1.90667713	0.46	0.40
KN5	5	25	0.160	2.5	1.420631883	0.46	0.60
B1	2	4	0.200	5.5	4.44130682	0.40	0.70
H1	2	4	0.001	1.0	0.9834230800463403	3.25	0.04
DB105	2	4	0.160	2.5	2.367027589	0.42	0.40
DN81	5	25	0.200	2.5	1.51408616	0.42	0.60
KN6	5	25	0.160	2.5	2.01304781	0.42	0.40
B	2	4	0.200	5.5	4.43357173	0.42	0.70
H	2	4	0.100	1.795	1.7907654704	0.42	0.40

gard to the thin and the thick + thin disk, the above mentioned values are changed in some models (DN81, KN4, KN5, KN6) for improving the fit to the data. The maximum normalized oxygen abundance during the (L_C+1)-th step, $\phi^*_{\rm max}$, is fixed by the boundary condition of equal IMF during and after the assembling phase. The effective yield to the true yield ratio, $\hat{p}''/\hat{p}$, and the slope of the TDOD of the adjoint simple homogeneous model, a, have been selected within a narrow range, outside which no acceptable fit to the data has been found. More specifically, the following considerations can be made.

The lower and upper normalized oxygen abundance limit, $\phi_{\rm min}$ and $\phi_{\rm max}$, have to be conceived as boundary conditions with respect to the subsystem under consideration. Assuming, say, $\phi_{\rm min} = 0$, would be meaningless in that (i) no star with zero metallicity has still been detected, and (ii) it would imply a G-dwarf problem in absence of ad hoc assumptions. Values $(\phi_{\rm min}, \phi_{\rm max}) = (0.16, 2.5)$ for the SN thick disk, $(0.4, 3.2)$ for the SN thin disk, $(0.16, 3.2)$ for the SN thick + thin disk, $(0.001, 1.0)$ for the SN halo, $(0.2, 5.5)$ for the bulge are taken from the most populated sample from which the EDOD has been deduced. Values $(0.2, 2.5)$ for the SN thin disk and $(0.16, 2.5)$ for the SN thick + thin disk are obtained by removing a single oxygen overabundant star (HIP68184) from the RaN07 subsample and, in the former case, assuming the low-metallicity tail of SN (still undetected) thin disk stars extends down to $\phi = 0.2$. Values $(0.1, 1.795)$ for the SN inner halo are taken from the incomplete RaH07 subsample, which makes the associated model poorly representative, even if conceptually interesting.

The maximum normalized oxygen abundance during the $(L_{\rm C} + 1)$-th step, $\phi^*_{\rm max}$, defines the IMF during (first $L_{\rm C}$ steps) and after (subsequent $L_{\rm A} - L_{\rm C}$ steps) the assembling phase. The high number of digits ensures the same IMF during the whole evolution. It can be seen that the same number of steps during and after the assembling phase, has been assigned to both the SN thick disk, the SN halo, and the bulge, on one hand, and to both the SN thin and the SN thick + thin disk, on the other hand. Strictly speaking, it would not imply a similar formation timescale, as suggested by recent findings (e.g., Melendez et al. (2008)): to this aim, an equal duration would also be assigned to each step, which is relevant in dealing with the age-metallicity relation, but leaves the TDOD unchanged.

The remaining input parameters are the effective to true yield ratio, $\hat{p}''/\hat{p}$, and the product:

$$-a\frac{\hat{p}''}{\hat{p}} = \frac{(Z_{\rm O})_\odot}{\ln 10}\frac{1}{\hat{p}} \quad ; \qquad (6)$$

which is inversely proportional to the true yield. For further details refer to parent papers (C00, C01, C07).

Values of output parameters for models shown in Table 7 are listed in Tables 8 and 9, respectively. Additional cases where gas in neither inhibited from, nor enhanced in, star formation, are listed in Table 10. The meaning of the parameters is explained in Appendix A. For further details refer to parent papers (C00, C01, C07).

The TDOD related to models DB15 and DN is compared in Fig. 1 to the corresponding EDOD with regard to SN thick (RaK07 subsample, left panels) and SN thin (RaN07 subsample, right panels) disk stars, respectively, both in presence (top panels) and in absence (bottom panels) of the LTE approximation. On each panel, the fit to the data is plotted as a full curve, and its counterpart related to the right or left panel as a dashed line for comparison. Models are fitted to NLTE data.

The TDOD related to models DB15, DN81, KN4, and B, is compared in Fig. 2 to the corresponding EDOD with regard to SN thick disk (MaK08 subsample, top left), SN thin disk (MaN08 subsample, top right), SN thick + thin disk [MaK08 + MaN08 subsample with assumed $M_{\rm KD}/M_{\rm ND} = 0.1$ (diamonds) and 0.9 (triangles), bottom left], and bulge (MaB08 subsample, bottom right) stars, respectively. On each panel, the fit to the data is plotted as a full curve, and its counterpart related to the right or left panel as a dotted line for comparison. Model B1 is represented by the dashed curve (bottom right).

The TDOD related to models DB15 (full), DN (dot-dashed), B1 (dotted), and H1 (dashed), is compared in Fig. 3 to the corresponding EDOD with regard to SN uncertain population (RaU07 subsample, left panels) and SN halo (RaH07 subsample, right panels) stars, respectively, both in presence (top panels) and in absence (bottom panels) of the LTE approximation.

The TDOD related to models KN2 (dashed) and KN3 (full) is compared in Fig. 4 to the corresponding EDOD, with regard to SN thick + thin disk (RaK07 + RaN07 subsample) stars for assumed SN thick to thin disk mass ratio, $M_{\rm KD}/M_{\rm ND} = 0.1$ (triangles), 0.3 (diamonds), 0.5 (crosses), 0.7 (squares), and 0.9 (asterisks). Both error bars and TDODs are omitted in right panels to gain clarity. Model DB105, related to the SN thick disk, is also represented as a dotted line. The dashed vertical bands correspond to [Fe/H]$= -1$ and related uncertainties, according to Eq. (4), with regard to a thick disk (left) and a thin disk (right) subsample (Ramirez et al. (2007)). Models are fitted to NLTE data.

The TDOD related to models DB12, DB13, DB14, DB15, DB105 (from up to down along the vertical line,

Table 8 Values of output parameters related to the expected evolution of inhomogeneous simple models, for four different cases concerning the thick disk (models DB), and five concerning the thin disk (models DN), respectively. The indices, 2.9 and 2.35, denote values related to the power-law IMF exponent, p, in computing the corresponding quantities. For the parameter, ψ_1, upper and lower values are calculated as in an earlier attempt (C07) by use of Eqs. (40) and (41) therein, respectively. The effective yield, $\hat{p}'$, is related to inhomogenities in oxygen abundance due to the presence of active and quiescent regions, whereas oxygen is uniformly distributed within active regions. The lower part of the Table (last 6 rows) is related to models with inhibited star formation. Parameters not reported therein have the same value as in the upper part, with the exception of $\hat{p}$, α, and $\widetilde{m}_{\rm mf} = m_{\rm mf}/{\rm m}_\odot$, which are listed in Table 10 together with other parameters not appearing here. The effective yield, $\hat{p}''$, due to the presence of (inhibiting star formation) gas within active regions, is listed as $\hat{p}$ in the upper part of the table. The effective yield, $\hat{p}'$, due to the presence of both (inhibiting star formation) gas within active regions, and (precluding star formation) gas within quiescent regions, is listed with the same notation in the upper part of the table. The index, R, denotes a generic active region. The mean oxygen abundance (normalized to the solar value) of stars at the end of evolution is denoted as $\overline{\phi}$

	LTE				NLTE			
	DB12	DB13	DB14	DB15	DN	DN4	DN5	DN6
$\mu'_{\rm R}$	1.3243 E−1	1.2295 E−1	1.1258 E−1	1.0304 E−1	1.6663 E−1	3.7477 E−1	3.6662 E−1	3.5864 E−
q	6.1771 E−1	5.5533 E−1	4.9941 E−1	4.4924 E−1	8.0550 E−1	9.6146 E−1	9.3741 E−1	9.1396 E−
χ	4.4156 E−1	5.0700 E−1	5.6410 E−1	6.1403 E−1	2.3339 E−1	6.1635 E−2	9.8821 E−2	1.3416 E−
$\hat{p}/(Z_{\rm O})_\odot$	9.0478 E−1	8.3518 E−1	7.7553 E−1	7.2382 E−1	7.2382 E−1	1.8096 E−0	1.4476 E−0	1.2064 E−
$\hat{p}'/(Z_{\rm O})_\odot$	3.6191 E−1	3.3407 E−1	3.1021 E−1	2.8953 E−1	2.8953 E−1	1.0857 E−0	8.6859 E−1	7.2382 E−
μ_f	1.4559 E−1	9.5108 E−2	6.2204 E−2	4.0731 E−2	4.4842 E−3	3.7439 E−1	1.9872 E−1	1.0548 E−
$\alpha_{2.9}$	6.9505 E−1	7.1175 E−1	7.2671 E−1	7.4020 E−1	7.4020 E−1	5.3263 E−1	5.8755 E−1	6.3092 E−
$\alpha_{2.35}$	8.6951 E−1	8.7833 E−1	8.8803 E−1	8.9281 E−1	8.9281 E−1	7.6914 E−1	8.0638 E−1	8.3327 E−
$(\widetilde{m}_{\rm mf})_{2.9}$	4.0227 E−1	3.7813 E−1	3.5660 E−1	3.3728 E−1	3.3728 E−1	6.4228 E−1	5.6022 E−1	4.9602 E−
$(\widetilde{m}_{\rm mf})_{2.35}$	1.1305 E−2	9.3463 E−3	7.8194 E−3	6.6108 E−3	6.6108 E−3	5.1835 E−2	3.2618 E−2	2.1898 E−
$\Delta^*\phi$	1.7435 E−1	1.9650 E−1	2.1539 E−1	2.3168 E−1	6.2622 E−2	4.2667 E−2	5.6142 E−2	6.5123 E−
$\Delta^*\phi'_{\rm R}$	1.8170 E−0	1.7505 E−0	1.6938 E−0	1.6450 E−0	1.2971 E−0	1.7760 E−0	1.4526 E−0	1.2370 E−
$-\psi_o$	2.4322 E−1	1.7337 E−1	1.1035 E−1	5.3384 E−2	4.8961 E−2	1.2641 E−0	1.0696 E−0	9.0546 E−
$-\psi_1(40)$	2.8439 E−1	2.2346 E−1	1.6926 E−1	1.2104 E−1	5.0826 E−1	1.2692 E−0	1.0780 E−0	9.1713 E−
$-\psi_1(41)$	2.8506 E−1	2.2446 E−1	1.7066 E−1	1.2289 E−1	5.0839 E−1	1.2692 E−0	1.0780 E−0	9.1718 E−
κ	1.4286 E−1	2.3810 E−1	3.3333 E−1	4.2857 E−1	4.2857 E−1	−4.2857 E−1	−2.8571 E−1	−1.4286 E−
$s'_{\rm R}$	7.5755 E−1	7.0839 E−1	6.6557 E−1	6.2787 E−1	5.8336 E−1	1.0942 E−0	8.8673 E−1	7.4825 E−
$D'_{\rm R}$	1.0822 E−1	1.6866 E−1	2.2186 E−1	2.6909 E−1	2.5001 E−1	−4.6892 E−1	−2.5335 E−1	−1.0689 E−
$\overline{\phi}$	7.8307 E−1	7.4978 E−1	7.2065 E−1	6.9485 E−1	8.6448 E−1	1.1450 E−0	1.0068 E−0	9.1462 E−
s_f	7.4761 E−1	7.3087 E−1	7.0335 E−1	6.7149 E−1	6.9686 E−1	1.0948 E−0	1.1218 E−0	1.0436 E−
D_f	1.0680 E−1	1.7402 E−1	2.3445 E−1	2.8778 E−1	2.9865 E−1	−4.6921 E−1	−3.2051 E−1	−1.4909 E−

Table 9 Values of output parameters related to the expected evolution of inhomogeneous simple models, for five different cases concerning the thick + thin disk (models KN). Additional cases related to the bulge (model B1) and the halo (model H1), taken from an earlier attempt (C07), but related to a different reference model with respect to inhibition from and enhancement in star formation, are listed for comparison. Captions as in Table 8

	KN1	KN2	KN3	KN4	KN5	B1	H1
μ'_{R}	1.7520 E−1	1.6240 E−1	3.4073 E−1	1.8550 E−1	3.5544 E−1	1.4139 E−1	8.2201 E−4
q	8.5730 E−1	7.8025 E−1	8.6171 E−1	9.2064 E−1	9.0458 E−1	2.4833 E−1	4.4991 E−2
χ	1.7302 E−1	2.6236 E−1	2.0977 E−1	9.7438 E−2	1.4804 E−1	8.7545 E−1	9.5579 E−1
$\hat{p}/(Z_{\mathrm{O}})_\odot$	9.4412 E−1	7.2382 E−1	9.4412 E−1	9.4412 E−1	9.4412 E−1	1.0857 E−0	1.3363 E−1
$\hat{p}'/(Z_{\mathrm{O}})_\odot$	3.7765 E−1	2.8953 E−1	5.6647 E−1	3.7765 E−1	5.6647 E−1	7.6001 E−1	5.3452 E−3
μ_f	2.1295 E−2	2.0221 E−3	2.4210 E−2	1.2653 E−1	8.1501 E−2	3.8030 E−3	4.0973 E−6
$\alpha_{2.9}$	6.8596 E−1	7.4020 E−1	6.8596 E−1	6.8596 E−1	6.8596 E−1	6.5510 E−1	9.3915 E−1
$\alpha_{2.35}$	8.6460 E−1	8.9281 E−1	8.6460 E−1	8.6460 E−1	8.6460 E−1	8.4739 E−1	9.7832 E−1
$(\widetilde{m}_{\mathrm{mf}})_{2.9}$	4.1547 E−1	3.3728 E−1	4.1547 E−1	4.1547 E−1	4.1547 E−1	4.6050 E−1	6.7781 E−2
$(\widetilde{m}_{\mathrm{mf}})_{2.35}$	1.2495 E−2	6.6108 E−3	1.2495 E−2	1.2495 E−2	1.2495 E−2	1.7263 E−2	7.5651 E−5
$\Delta^*\phi$	5.8147 E−2	7.1945 E−2	8.4313 E−2	3.1228 E−2	5.6809 E−2	1.0587 E−0	1.6577 E−2
$\Delta^*\phi'_{\mathrm{R}}$	1.6445 E−0	1.3157 E−0	1.0165 E−0	1.5905 E−0	9.7659 E−1	2.1239 E−0	9.4927 E−1
$-\psi_o$	7.2759 E−1	4.3986 E−1	6.4265 E−1	9.2754 E−1	7.6772 E−1	9.1837 E−2	8.5447 E−1
$-\psi_1(40)$	7.4089 E−1	4.6123 E−1	6.6189 E−1	9.3471 E−1	7.8072 E−1	2.8650 E−1	8.2781 E−1
$-\psi_1(41)$	7.4096 E−1	4.6141 E−1	6.6204 E−1	9.3473 E−1	7.8079 E−1	3.0358 E−1	8.2753 E−1
κ	9.5238 E−2	4.2857 E−1	9.5238 E−2	9.5238 E−2	9.5238 E−2	−4.7619 E−2	6.7381 E−0
s'_{R}	7.5307 E−1	5.8632 E−1	6.0194 E−1	7.4367 E−1	5.8851 E−1	9.0154 E−1	1.2912 E−1
D'_{R}	7.1721 E−2	2.5128 E−1	5.7327 E−2	7.0826 E−2	5.6048 E−2	−4.2930 E−2	8.7005 E−1
$\overline{\phi}$	7.5480 E−1	6.2873 E−1	5.7876 E−1	7.4187 E−1	5.6558 E−1	9.3597 E−1	1.3385 E−1
s_f	8.9360 E−1	6.9858 E−1	8.9094 E−1	7.9751 E−1	8.3863 E−1	1.0460 E−0	1.2923 E−1
D_f	8.5105 E−2	2.9939 E−1	8.4851 E−2	7.5954 E−2	7.9869 E−2	−4.9810 E−2	8.7077 E−1

Table 10 Values of output parameters related to the expected evolution of inhomogeneous simple models, for five different cases concerning the thick disk (model DB105), the thin disk (model DN81), the thick + thin disk (model KN6), the bulge (model B), and the inner halo (model H). The stellar initial mass function (IMF) is strictly universal, in the sense that neither inhibition from, nor enhancement in, star formation, appear in one model with respect to the other. Captions as in Table 8

	DB105	DN81	KN6	B	H
$\mu'_{\rm R}$	1.5302 E−1	3.6062 E−1	1.8860 E−1	1.3113 E−1	1.9653 E−1
q	7.2507 E−1	9.1977 E−1	9.3992 E−1	2.2916 E−1	9.8981 E−1
χ	3.2460 E−1	1.2549 E−1	7.4049 E−2	8.8717 E−1	1.2677 E−2
$\hat{p}/(Z_{\rm O})_\odot$	1.0340 E−0	1.0340 E−0	1.0340 E−0	1.0340 E−0	1.0340 E−0
$\hat{p}'/(Z_{\rm O})_\odot$	4.1361 E−1	6.2042 E−1	4.1361 E−1	7.2382 E−1	4.1361 E−1
μ_f	2.7639 E−1	1.2357 E−1	2.1244 E−1	2.7579 E−3	9.5988 E−1
$\alpha_{2.9}$	6.6604 E−1	6.6604 E−1	6.6604 E−1	6.6604 E−1	6.6604 E−1
$\alpha_{2.35}$	8.5360 E−1	8.5360 E−1	8.5360 E−1	8.5360 E−1	8.5360 E−1
$(\widetilde{m}_{\rm mf})_{2.9}$	4.4449 E−1	4.4449 E−1	4.4449 E−1	4.4449 E−1	4.4449 E−1
$(\widetilde{m}_{\rm mf})_{2.35}$	1.5436 E−2	1.5436 E−2	1.5436 E−2	1.5436 E−2	1.5436 E−2
$\Delta^*\phi$	1.3297 E−1	5.1890 E−2	2.5629 E−2	1.0664 E−0	4.2345 E−3
$\Delta^*\phi'_{\rm R}$	1.9411 E−0	1.0546 E−0	1.7249 E−0	2.1007 E−0	1.6823 E−0
$-\psi_o$	3.6269 E−1	8.5864 E−1	1.0413 E−0	6.5328 E−2	5.1492 E−1
$-\psi_1(40)$	3.9032 E−1	8.6950 E−1	1.0467 E−0	2.7020 E−1	5.1581 E−1
$-\psi_1(41)$	3.9062 E−1	8.6954 E−1	1.0467 E−0	2.8928 E−1	5.1581 E−1
κ	0.0000 E−0	0.0000 E−0	0.0000 E−0	0.0000 E−0	0.0000 E−0
$s'_{\rm R}$	8.4698 E−1	6.3938 E−1	8.1140 E−1	8.6887 E−1	8.0347 E−1
$D'_{\rm R}$	0.0000 E−0	0.0000 E−0	0.0000 E−0	0.0000 E−0	0.0000 E−0
$\overline{\phi}$	8.4335 E−1	6.3920 E−1	7.9310 E−1	9.1700 E−1	7.2253 E−1
s_f	7.2361 E−1	8.7643 E−1	7.8756 E−1	9.9724 E−1	4.0244 E−2
D_f	0.0000 E−0	0.0000 E−0	0.0000 E−0	0.0000 E−0	0.0000 E−0

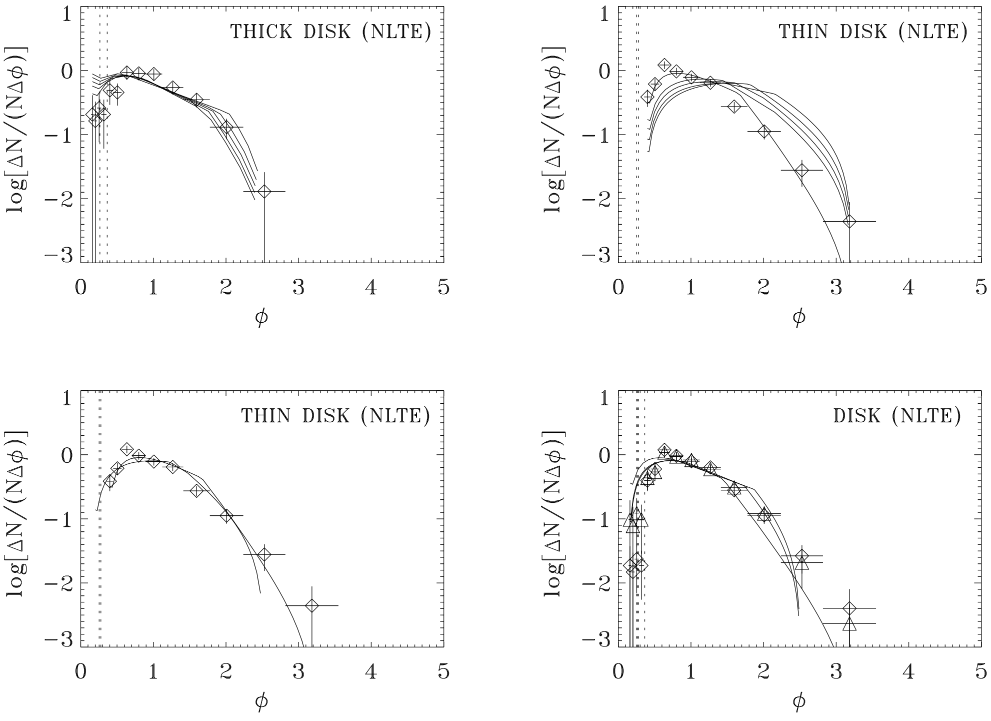

Fig. 5 The empirical, differential oxygen abundance distribution (EDOD) related to the RaK07 (top left), RaN07 (top right and bottom left) and RaK07 + RaN07 (bottom right) subsample, for assumed SN thick to thin disk mass ratio, $M_{\mathrm{KD}}/M_{\mathrm{ND}} = 0.1$ (diamonds) and 0.9 (triangles), in absence of the local thermodynamic equilibrium (LTE) approximation. The theoretical, differential oxygen abundance distribution (TDOD) related to inhomogeneous models of chemical evolution, is plotted for the following models: DB12, DB13, DB14, DB15, DB105 (from up to down along the vertical line, $\phi = 2.0$, top left); DN4, DN5, DN6, DN7, DN (from up to down along the vertical line, $\phi = 2.5$, top right); DN, DN81 (from up to down along the vertical line, $\phi = 2.4$, bottom left); KN2, KN4, KN6 (from down to up along the vertical line, $\phi = 2.0$, bottom right). The dashed vertical bands correspond to [Fe/H]$= -1$ and related uncertainties, deduced from Eq. (4) with regard to a thick disk (upper left and lower right) and a thin disk (upper right and bottom panels) subsample (Ramirez et al. (2007))

$\phi = 2.0$, top left); DN4, DN5, DN6, DN7, DN (from up to down along the vertical line, $\phi = 2.5$, top right); DN, DN81 (from up to down along the vertical line, $\phi = 2.4$, bottom left); KN2, KN4, KN6 (from down to up along the vertical line, $\phi = 2.0$, bottom right); is compared in Fig. 5 to the corresponding EDOD with regard to SN thick disk (RaK07 subsample, top left), SN thin disk (RaN07 subsample, top right and bottom left), and SN thick + thin disk [RaK07 + RaN07 subsample with assumed $M_{\mathrm{KD}}/M_{\mathrm{ND}} = 0.1$ (diamonds) and 0.9 (triangles), bottom right] stars, respectively, in absence of the LTE approximation.

5 Discussion

5.1 Fitting empirical differential oxygen abundance distributions

Acceptable fits to the EDOD related to SN thin or thick + thin disk stars, must satisfy the boundary condition of a nonnegligible present-day gas mass fraction, $\mu_f = M_{\mathrm{g}}/M = 0.1$-$0.3$ (e.g., Prantzos and Aubert (1995)). Accordingly, related models (DN and KN, respectively) must be disregarded if (i) the EDOD is poorly fitted and/or (ii) μ_f lies outside the above mentioned range.

With regard to the SN thin disk, an inspection of Figs. 1, 3, 5 and Table 8 shows that the sole acceptable model (DN81) needs lowered initial and final oxygen abundance, close to thick disk values. More specifically, fitting the data implies the existence of SN thin disk stars with normalized oxygen abundance down to $\phi \approx 0.2$ and, in addition, the removal of a single oxygen overabundant ($[\mathrm{O/H}]_{\mathrm{NLTE}} = 0.48$ or $\phi \approx 3$) star (HIP68184) from the sample, which could be due to peculiar evolutionary effects and/or systematic errors. In the light of the model, the following conclusion holds: if the thick and the thin disk evolved as separate entities, the chemical evolution spanned along a similar oxygen abundance range.

With regard to the SN thick + thin disk, an inspection of Fig. 5 and Table 9 shows that the two acceptable models (KN4 and KN6) need lowered final oxygen abundance, close to thick disk values. More specifically, fitting the data implies the removal of the above mentioned, oxygen overabundant star, from the sample. In the light of the model, the following conclusion holds: if the thick and the thin disk evolved as a single entity, the chemical evolution spanned along a similar oxygen abundance range with respect to the thick disk considered alone. Models where the thick and the thin disk evolve as a whole, are consistent with the existence of an evolutionary link between the two disk components (Haywood (2008)). It is worth remembering that the above quoted paper is referring to a kinematic evolution or migration between thin and thick disks, as opposed to some form of Galactic chemical evolution.

With regard to the bulge, an inspection of Figs. 2, 3 and Tables 9, 10 shows that both the models considered (B and B1) provide acceptable fits to bulge and SN halo data, with negligible amount of gas left at the end of evolution, as expected. In the light of the model, the following conclusion holds: oxygen production within the bulge and the SN halo underwent a similar history for the common abundance range. This result is highly speculative, due to the incompleteness of the halo sample from which the data were extracted (Ramirez et al. (2007)).

With regard to the SN halo, an inspection of Fig. 3 and Tables 9, 10 shows that a fraction of low-metallicity data is fitted by a single model (H1), while the remaining part is fitted by a second model (H). Accordingly, the (incomplete) halo sample from which the data were extracted (Ramirez et al. (2007)) has to be conceived as made of two distinct classes of objects, namely (i) stars from a gas reservoir from which both the inner halo, the bulge, and the thick disk originated, and (ii) stars from a gas reservoir from which the outer halo originated. In the light of the model, the following conclusion holds: oxygen production within the SN inner halo, the bulge, and the thick disk underwent a similar history for the common abundance ranges, while the chemical evolution of the SN outer halo was different. In fact, input parameters related to the outer halo model (H1) are markedly different from the remaining ones, as shown in Table 7. A stellar dichotomy between the inner and the outer halo has recently been detected (Carollo et al. (2007)).

The assumption of universal IMF implies gas inhibition from, or enhancement in, star formation, with respect to a reference thin disk model (C07, C08), which has been chosen to be DN81. Then a legitimate question is about the existence of models which fit to an acceptable extent the EDOD related to the SN thick disk, SN thin disk, SN inner halo, bulge, and where, in addition, gas is neither inhibited from, nor enhanced in, star formation. The answer is positive, as shown in Table 10 and Figs. 2, 3, and 5.

For a specified universal IMF, the key parameter appears to be the probability of a region being active, χ. The chemical evolution of the SN thick, thin, and thick + thin disk, appear to be characterized by low values, $\chi = 0.32$, 0.13, 0.07, respectively, while a high value, $\chi = 0.89$, is related to the chemical evolution of the bulge, as shown in Table 10. In addition, the chemical evolution of the SN inner halo is characterized by $\chi = 0.013$, a value close to one tenth its SN thin disk counterpart. The corresponding true oxygen yield, $\hat{p} = 0.0058$, is consistent with $\hat{p} = 0.0085 \mp 0.0035$ deduced from observations (e.g., Prantzos (1994)).

In conclusion, a single inhomogeneous model of chemical evolution with universal IMF and gas neither inhibited from, nor enhanced in, star formation, provides acceptable fits to the EDOD related to both the SN inner halo, the SN thick disk, the SN thin disk, the SN thick + thin disk, and the bulge. In particular, the main part of objects of uncertain population could belong to the thin disk, as shown in Fig. 3. Conversely, an inhomogeneous model with considerable amount of gas inhibited from star formation (H1), used in an earlier attempt (C07), provides an acceptable fit to the outer halo.

With regard to the SN thick disk, the SN thin disk, and the bulge, both poor and rich samples are fitted by the same models. With regard to the SN halo, the existence of two different classes of objects in the (incomplete) related sample, has to be advocated: a low-metallicity tail belonging to the outer halo, and a higher-metallicity body belonging to the inner halo, each fitted by a different model, as shown in Fig. 3. A possible explanation shall be given below.

5.2 A physical interpretation of the model

The EDODs related to MaK08, MaN08, MaK08 + MaN08, MaB08, RaK07, RaN07, RaK07 + RaN07 subsamples, are fitted to an acceptable extent by models DB105, DN81, KN6, B, listed in Table 10. In addition, the EDOD related to the RaH07 subsample is fitted to an acceptable extent by model H listed in Table 10, provided the low-metallicity tail is not considered. Present-day gas mass fraction and oxygen abundance related to the SN disk may be expressed as weighted means:

$$\mu_f = \frac{M_{\rm g}}{M} = \frac{M_{\rm Kg}+M_{\rm Ng}}{M_{\rm K}+M_{\rm N}}$$
$$= \frac{M_{\rm K}\mu_{\rm Kg}}{M_{\rm K}+M_{\rm N}} + \frac{M_{\rm N}\mu_{\rm Ng}}{M_{\rm K}+M_{\rm N}} \quad ; \qquad (7)$$

$$(Z_{\rm O})_f = \frac{(M_{\rm O})_{\rm g}}{M_{\rm g}} = \frac{(M_{\rm O})_{\rm Kg}+(M_{\rm O})_{\rm Ng}}{M_{\rm Kg}+M_{\rm Ng}}$$
$$= \frac{M_{\rm Kg}(Z_{\rm O})_{\rm Kg}}{M_{\rm Kg}+M_{\rm Ng}} + \frac{M_{\rm Ng}(Z_{\rm O})_{\rm Ng}}{M_{\rm Kg}+M_{\rm Ng}} \quad ; \qquad (8)$$

where $M_{\rm g}$ and M are the present gas and total mass, and the indices, K and N, denote the thick and the thin disk, respectively. For models DB105 and DN81, the reference values, $M_{\rm K}/M_{\rm N} = 0.1,\ 1$, yield $\mu_f = 0.13746$, 0.19998, respectively, to be compared to $\mu_f = 0.21244$ related to model KN6, where the thick and thin disk evolve as a single system.

Models listed in Table 10 are related to a strictly universal IMF, in the sense that both the power-law exponent and the upper and lower stellar mass limit coincide in all cases and, in addition, gas is neither inhibited from, nor enhanced in, star formation, concerning one model with respect to the other. This is a stronger condition in comparison with earlier results (C01, C07, C08) based on SN disk samples biased towards high-metallicity stars.

For models characterized by a strictly universal IMF, the probability of a region being active, χ, is highly relevant. An inspection of Table 10 shows that $\chi = 0.01268, 0.07405$, for the SN inner halo and the SN thick + thin disk, respectively, increasing up to $\chi = 0.12549$, 0.32460, 0.88717, for the SN thin disk, the SN thick disk, and the bulge, respectively. A physical interpretation of the above results, in the light of the model, is that the probability of a region being active mainly depends on the environment.

More specifically, the star formation rate within an active region is independent of the environment in the case under discussion. On the contrary, a different global efficiency (which is proportional to the probability of a region being active) takes place in different environments. Using the values of χ listed in Table 10, the following global efficiency ratios are calculated: $\chi_{\rm B}/\chi_{\rm H} \approx 70$; $\chi_{\rm B}/\chi_{\rm KN} \approx 12$; $\chi_{\rm B}/\chi_{\rm N} \approx 7$; $\chi_{\rm B}/\chi_{\rm K} \approx 3$; where B, H, K, N, KN denote the bulge, the SN halo, the SN thick disk, the SN thin disk, the SN thick + thin disk, respectively.

Star formation is triggered by tidal interaction (including merging, which can be conceived as the strongest tidal interaction). Accordingly, lower χ values are expected in environments where tidal effects are poorly experienced, such as the inner halo, the thick + thin disk, and the thin disk. On the other hand, larger χ values are expected in environments where considerable tidal effects take place, such as the thick disk and the bulge. According to recent findings (e.g., Melendez et al. (2008)) the thick disk and the bulge formation timescales were similar, of the order of several tenths of Gyr. The density is higher at the end of contraction, which could maximize tidal effects between different regions, and then produce a larger number of active regions with respect to environments where the density is considerably lower (inner halo) or the chemical evolution timescale considerably longer (thin disk).

5.3 Universal IMF and G-dwarf problem

A different IMF in bulge and disk components has been advocated for explaining the metallicity distribution in both the Milky Way and Andromeda bulge (Ballero et al. (2007b)), contrary to what has been deduced from recent observations performed on SN thick disk, SN thin disk, and Milky Way bulge stars (Melendez et al. (2008)). As pointed out in an earlier attempt (C08), a large fraction of Fe production depends on type Ia supernovae which, in turn, are thought to be born from an accreting white dwarf progenitor in a binary system, including a red giant outside its Roche lobe. Accordingly, different IMFs in different environments could be simulated by different amounts of binary star fractions (in particular, SnIa progenitors). In this view, denser environments where objects with opposite velocity vectors are close one to the other (e.g., the assembling bulge, the assembling thick disk) should be expected to exhibit a smaller binary star fraction (in particular, SnIa progenitors), with respect to less dense environments where objects with parallel velocity vectors are close one to the other (e.g., the assembled thin disk).

Regions undergoing an early infall phase (of primordial composition), with the smaller regions having a more important infall, have been advocated for explaining the field star metallicity distribution in both the halo and dwarf spheroidal satellites of the Milky Way, where a G-dwarf problem seems to occur (Prantzos (1994)). Though a G-dwarf problem (i.e. overabundance of low-metallicity, long-lived stars predicted by the Simple model with respect to observations) has been detected both in bulge-dominated and disk-dominated galaxies (Henry and Worthey (1999)) and is probably universal (Worthey et al. (1996)), still it may be explained by a large number of different ways (e.g., Pagel and Patchett (1975)) including, among others, unprocessed gas inflow. On the other hand, a prompt initial enrichment from pop. III stars cannot be overlooked and, in particular, the idea of a coeval formation of pop. III and pop. II stars cannot be disregarded (e.g., Smith et al. (2008)). In this view, the G-dwarf problem in old stellar systems (e.g., the halo) could find a natural explanation, if still occurring within the framework of inhomogeneous models of chemical evolution.

5.4 Stellar migration across the disk

Though sample objects considered in the current paper, with the exception of bulge stars, are made of SN stars, still related informations provide valuable clues for understanding the formation process of the Galaxy. The assumption that the EDOD of the local disk is representative of the global disk, even if in contrast with an inside-out disk formation, can be considered as a useful zero-th order approximation. On the other hand, nearby stars older than about 0.2 Gyr come from birth sites which span a large range in Galactocentric distances (e.g., Rocha-Pinto et al. (2000)). The orbital diffusion coefficient deduced from the observed increase of velocity dispersion with age implies that presently local stars have suffered a rms azimuthal drift from about 2 kpc (for an age of 0.2 Gyr) to many Galactic orbits (for an age of 10 Gyr); for further details refer to earlier work (Wielen (1977)). Considerable, but smaller, drift should occur also on the radial direction (Wielen et al. (1996); Haywood (2008)).

In this sense, the star formation rate inferred for nearby stars is a measure of the global Milky Way star formation rate, at least at the sun Galactocentric radius (Rocha-Pinto et al. (2000)), according to the estimates of the diffusion coefficient (e.g., Meusinger et al. (1991)). Star migration along the equatorial plane is mainly due to churning and blurring via interactions between stars and spiral arms (Sellwood and Binney, 2002; Schönrich and Binney (2009)). Diffusion calculations based on the increase of local velocity dispersion with age, could be inaccurate if significant migration occurs, as due to resonant scattering with transient spiral arms, which makes local samples considerably affected by radial migration, according to N-body + smooth particle hydrodynamics simulations (Roškar et al. (2008)).

As outlined in an earlier attempt (Wang and Silk (1993)), radial flows of the gas (possibly due to the observed spiral density waves) or different disk star formation histories (with time scales comparable to that of chemical evolution) between the inner and the outer parts of the Galaxy, may change the local abundances, but the overall abundance in the disk should not be affected as long as there is no gain or loss of material in the disk. It can also be noticed (Wang and Silk (1993)) that the average oxygen abundance in the disk is roughly the solar value, and can be plausibly explained by the standard Scalo IMF with lower and upper star mass limit, $\widetilde{m}_{\rm mf} = 0.1$ and $\widetilde{m}_{\rm Mf} = 60$, respectively, or by a power-law IMF with exponent, p, within the range, $2.35 \le p \le 2.9$, and the same $\widetilde{m}_{\rm mf}$ and $\widetilde{m}_{\rm Mf}$. For further details refer to the parent paper (Wang and Silk (1993)).

Inhomogeneous models can describe to some extent stellar migration across the disk, provided inflow (i.e. enhanchement of star formation) is considered. As outlined in an earlier attempt (C07), inhomogeneous models where star formation is enhanced imply star inflow with same oxygen abundance as in the existing gas, which mimics (a special case of) stellar migration. Mass conservation no longer holds, and the effective gas mass fraction (normalized to the final mass), $\mu_{\rm eff}$, is expressed in terms of the actual gas mass fraction (normalized to the initial mass), μ, as:

$$\mu_{\rm eff} = \frac{\mu}{1+s_{\rm mig}} \quad ; \tag{9}$$

where $s_{\rm mig}$ is the inflowed star mass fraction (normalized to the initial mass), to be interpreted as the net stellar migration within the volume under consideration, i.e. the difference between the fractional mass in stars which have been born elsewhere and migrated inside, and born inside and migrated elsewhere, respectively.

In the framework of inhomogeneous models with enhanced star formation, the fractional mass in migrated stars is proportional to the fractional mass in stars generated in situ, $s_{\rm mig} = \zeta s = \zeta(1-\mu)$, and Eq. (9) may be rewritten as:

$$\mu = \frac{(1+\zeta)\mu_{\rm eff}}{1+\zeta\mu_{\rm eff}} \quad ; \tag{10}$$

where the effective gas mass fraction, $\mu_{\rm eff}$, can be deduced from the observations. For the solar neighbourhood, $0.1 \lesssim \mu_{\rm eff} \lesssim 0.3$ (Prantzos and Aubert (1995)), $\zeta \approx 1$ from high-resolution N-body + smooth particle hydrodynamics simulations of disk formation (Roškar et al. (2008)), and Eq. (10) yields $0.18 \lesssim \mu \lesssim 0.46$.

On the other hand, model DN4 listed in Table 8 produces $\mu \approx 0.37$, $s = 1-\mu \approx 0.63$ and and $-D_f = s_{\rm mig} \approx 0.47$, which implies about three quarters of stars were born in situ, and the remaining quarter is the net effect of stellar migration. Accordingly, inhomogeneous models with enhanced star formation provide an acceptable description of stellar migration even if, in the case considered, model DN4 fails in fitting the SN thin disk EDOD, as shown in Fig. 5 (top right panel).

5.5 Implications for the formation of the Galaxy

According to a number of recent investigations, the formation of the Galaxy appears to be characterized by the following main features.

(i) Thick disk stars had a chemical enrichment similar and coeval to metal-rich halo stars, $[\mathrm{Fe/H}] \approx -1.3$ (Prochaska et al. (2000)), $-1.5 < [\mathrm{Fe/H}] < -0.1$ (Ramirez et al. (2007)), $-1.3 < [\mathrm{Fe/H}] < -0.5$ (Melendez et al. (2008)).

(ii) Thick disk stars had a chemical enrichment similar and coeval to metal-poor bulge stars, $[\mathrm{Fe/H}] \lesssim -0.4$ (Prochaska et al. (2000)), $-1.3 < [\mathrm{Fe/H}] \leq -0.5$ (Melendez et al. (2008)).

(iii) The thick disk low-metallicity tail ends near $[\mathrm{Fe/H}] = -2.2$ (Chiba and Beers (2000)).

(iv) The bulge formation timescale is about 1 Gyr at most (Zoccali et al. (2008)).

(v) The halo is made of two broadly overlapping structural components: an inner halo with axis ratio close to 0.6, modest net prograde rotation, and peak metallicity at $[\mathrm{Fe/H}] = -1.6$; and an outer halo with nearly spherical shape, net retrograde rotation, and peak metallicity at $[\mathrm{Fe/H}] = -2.2$ (Carollo et al. (2007)).

(vi) The mean rotational velocities are close to zero or negative for the outer halo ($R \gtrsim 12\,\mathrm{kpc}$), which may correspond to the radial limit of the rapidly rotating thick disk component (Chiba and Beers (2000); Carollo et al. (2007)).

(vii) A linear dependence of mean rotational velocities on the metallicity for $[\mathrm{Fe/H}] \gtrsim -1.6$, appears to be consistent with the contraction of the inner halo (Chiba and Beers (2000)) after an earlier assembling phase. Interestingly, the inner halo metallicity peaks around $[\mathrm{Fe/H}] \approx -1.6$ (e.g., Ryan and Norris (1991); Carollo et al. (2007); Prantzos (2008)).

(viii) The distribution of specific angular momentum appears to be consistent with both a halo-bulge and a thick disk-thin disk collapse, but not with a spheroid-disk collapse (Wyse and Gilmore (1992); Ibata and Gilmore (1995)).

At this point, the question arises if the above mentioned results are a natural consequence of the currently favoured theory of galaxy formation based on hierarchical assembly of cold dark matter haloes in presence of both baryonic matter and quintessence (e.g., Mota and van de Bruck (2004); Horellou and Berge (2005)). In the framework of QCDM models, the initial density perturbations in the early universe have larger amplitudes on smaller scales, which makes low-mass density perturbations turn around and recollapse first. Accordingly, star formation is expected to start therein. For further details refer to earlier attempts related to CDM scenarios (e.g., Caimmi (1997); Chiba and Beers (2000)).

Low-mass density perturbations lying within a large-mass density perturbation, may be considered as secondary peaks bound to a primary peak (e.g., Ryden (1988)). In particular, objects existing at present with Galactic mass are likely built up by the merging and accretion of smaller, less massive progenitors. It may safely be thought that these progenitors - at least in the denser regions of the universe - allow baryons to concentrate in their cores. This process takes place as an inevitable consequence of energy dissipation via radiative cooling and anelastic collisions, which does not carry significant amount of angular momentum.

Stellar systems (and sufficiently clumpy gas clouds) moving along highly eccentric and/or highly inclinated orbits, make angular momentum transport possible via quadrupole interaction. More specifically, angular momentum is transferred from the orbital motion of the tighly bound cores to the loosely bound outer halo particles as the cores sink into the centre of the forming halo. This loss of angular momentum by the cores, due to dynamical friction, will lead to a low specific angular momentum in the assembled galaxy, as seen in ellipticals. For further details refer to earlier attempts (Zurek et al. (1988); Bekki and Chiba (2000)). On the other hand, stellar systems formed from the gas heated in the course of merging and accretion, when a substantial fraction of peculiar energy has been dissipated, would maintain their specific angular momentum, as seen in disk galaxies.

In this view, the inner halo should have a flattened density distribution with a finite prograde rotation, conformly to observations (Chiba and Beers (2000); Carollo et al. (2007)), and the angular momentum distribution may be similar to its bulge counterpart (Wyse and Gilmore (1992)). The thick disk could have been accreted from the external part of the proto-Galaxy (e.g., Sommer-Larsen et al. (1997)), and its angular momentum distribution may be similar to its thin disk counterpart (Ibata and Gilmore (1995)). In other words, the inner halo and the bulge could take origin from the denser internal region of the initial density perturbation, where smaller spin growth via tidal interactions with neighbouring objects occurs, while the less dense external region, characterized by a larger spin growth, could be the progenitor of the thick and thin disk. The outer halo could be built up via accretion of smaller fragments or satellites even if, initially, bound to different peaks.

The building blocks of each subsystem may be conceived in a twofold manner, as lower mass overdensities which first decouple from the universe (progenitors of compact dwarf galaxies) from the cosmological side, and upper mass gas media which form stars (molecular clouds or proto-globular clusters) from the astrophysical side.

In the framework of inhomogeneous models of chemical evolution considered in the current paper, star formation takes place within a fixed fraction of identical regions. At the end of any step, the enriched gas of active regions is homogeneously mixed with the unprocessed gas of quiescent regions, and a new set of identical regions is produced, which makes the beginning of the subsequent step. Accordingly, the chemical enrichment history in different environments, is expected to be similar and even coeval for a strictly universal IMF. In fact, the total number of steps is an input parameter, but the duration of a step can freely be assigned (C00, C01, C07). For fiducial values of mass and radius related to the proto-bulge ($M = \mathrm{M}_{10}$, $R = 6\,\mathrm{kpc}$) and the proto-inner halo + disk ($M = 6\,\mathrm{M}_{10}$, $R = 15\,\mathrm{kpc}$), the free-fall time is 0.08-0.12 Gyr, a few times lower than the bulge formation timescale inferred from observations (Zoccali et al. (2008)).

Different environments could imply a different probability of a region being active i.e. a different ratio of active to active + quiescent regions at any step and, in turn, different global efficiencies of the star formation rate. In this sense, chemical evolution could be influenced by dynamical evolution: for instance, a higher number of active regions corresponds to environments where tidal effects between neighbouring regions are strong (e.g., the bulge) and vice versa (e.g., the halo).

Models implying large amount of gas inhibited from star formation (H1 in the current paper) succeed in reproducing (incomplete) data related to the outer halo population. To this respect, some considerations seem useful provided the fit shall be confirmed using richer samples. Even if mass conservation formally holds in models under discussion, the chemical evolution acts as gas inhibited from star formation and a fraction of gas synthesized in short-lived stars and returned to the interstellar medium, were lost from the outer halo and presumably accreted by the proto-Galaxy.

Using an outer halo star mass fraction, $s_f = 0.13$, inhibited (i.e. lost) gas mass fraction, $D_f = 0.87$, as listed in Table 9 for model H1, and assuming a stellar outer halo upper mass limit equal to $10^9\mathrm{m}_\odot$, the total mass lost from the outer halo cannot exceed $6.7\,10^9\mathrm{m}_\odot$. The total mass of the proto-Galaxy is about ten times larger, which makes little influence on the related chemical evolution. In conclusion, mass loss from active regions makes a different oxygen enrichment with respect to environments (inner halo, thick disk, thin disk, bulge) where mass conservation holds to a better extent.

The observed abundance distributions used in the current paper provide additional support to points (i), (ii), (iii), (v), listed above, where points (vi) and (vii) may be considered as complementary to (v). The comparison with model predictions, related to oxygen, is also consistent with the above mentioned points: the SN thick disk, the SN inner halo, and the bulge had similar and coeval oxygen enrichment within the common abundance range. On the other hand, a different model with gas inhibited from star formation has to be used for the outer halo, which is consistent with points (v), (vi), and (vii).

Keeping in mind point (iv), the above results imply a short formation timescale for both the (metal-rich) inner halo, the thick disk, the thin disk, and the bulge. Oxygen enrichment within a common range in different subsystems seems to be slightly dependent on dynamical parameters, according to point (viii). If any two subsystems formed on comparable timescales, as well as had a strictly universal IMF and star formation histories, the abundance pattern would be similar even if the two populations lack a physical connection.

An idea of how galaxies did form is offered by celestial bodies which are presently assembling i.e. cluster of galaxies. Similarly, individual proto-galaxies may be conceived as made of subunits (Still visible dwarf spheroidals? Subsequently dead dwarf spheroidals with surviving nuclei in form of globular clusters? Globular clusters?) which are virializing in the inner volume but are still falling in the outer volume, while a central structure (the proto-bulge) is growing up.

As outlined in an earlier attempt (Chiba and Beers (2000)), more elaborate numerical modelling of the formation of large spiral galaxies, such as the Milky Way, is also needed in order to clarify the physical processes that lead to the currently observed dynamics and structure of the spheroid and disk components. It is of particular importance to model and understand the chemodynamical evolution of the system of sub-galactic fragments in the course of the Galaxy assembling (e.g., Prantzos (1994)). A fundamental understanding of the formation and the evolution of the Milky Way, is expected to provide additional insights on the formation and the evolution of disk-type galaxies.

6 Conclusion

The main results of the present attempt may be summarized as follows.

(1) The empirical differential oxygen abundance distribution (EDOD) is determined from recent data involving different subsamples related to the solar neighbourhood (SN) halo, thick disk, thin disk, and to the bulge (Ramirez et al. (2007)); Melendez et al. (2008)).

(2) The EDOD related to different subsamples (including less recent ones) and/or different populations, show qualitative agreement above a threshold in iron abundance, [Fe/H]> -1, where the data in richer subsamples are statistically significant. The sole exception concerns halo stars, possibly due to subsample incompleteness (Ramirez et al. (2007)) and/or different halo populations (Carollo et al. (2007)).

(3) The SN thick + thin disk EDOD is deduced from its thick disk and thin disk counterparts, for different choices of the thick disk to thin disk mass ratio within the range, 0.1-0.9. The related effect is comparable to the error calculated for the EDOD.

(4) Inhomogeneous models with strictly universal initial mass function (IMF), implying gas is neither inhibited from, nor enhanced in, forming stars at different rates with respect to a selected reference case, provide an acceptable fit to the EDMD related to different environments. To this aim, a SN thin disk low-metallicity tail (down to $\phi \approx 0.2$) has to be assumed, and a single oxygen overabundant sample star must be disregarded as a peculiar object and/or affected by undetected systematic error. The existence of a strictly universal IMF implies a similar chemical enrichment within active regions placed in different environments which, on the other hand, exhibit increasing probability of a region being active, and then an increasing global efficiency of the star formation rate, passing from the SN halo to the SN thin disk, the SN thick disk, and the bulge. The evolution of the SN thick + thin disk as a whole (Haywood (2008)), computed using inhomogeneous models, is also consistent with the related EDMD.

(5) A special case of stellar migration across the disk (inflowing stars with equal oxygen abundance with respect to the existing gas) can be described by inhomogeneous models with enhanced star formation. In particular, values within the observed range in SN gas mass fraction may allow a fraction of present SN stars were born in situ, and a comparable fraction is due to the net effect of stellar migration, according to recent results based on high-resolution N-body + smooth particle hydrodynamics simulations (Roškar et al. (2008)).

Acknowledgements The authors are grateful to an anonymous referee for critical comments, which made substantial improvement of an earlier version of the paper. Thanks are due to R. Roškar for pointing our attention to a recent paper (Roškar et al. (2008)), quoted in the text.

References

Abia, C., Rebolo, R.: Astrophys. J. 347, 186 (1989)

Allende-Prieto, C., Lambert, D.L., Asplund M.: Astrophys. J. Lett. 556, L63 (2001)

Asplund, M., Grevesse, N., Sauval, A.J., et al.: Astron. Astrophys. 417, 751 (2004)

Ballero, S.K., Kroupa, P., Matteucci, F.: Astron. Astrophys. 467, 117 (2007a)

Ballero, S.K., Matteucci, F., Origlia, L., Rich, R.M.: Astron. Astrophys. 467, 123 (2007b)

Barbuy, B.: Astron. Astrophys. 191, 121 (1988)

Barbuy, B., Nissen, P.E., Peterson, R., Spite, F. (eds.), Proceedings of Oxygen abundances in old stars and implications for nucleosynthesis and cosmology (IAU Joint Discussion 8): New Astron. Rev. 45, 509 (2001)

Bekki, K., Chiba, M.: Astrophys. J. Lett. 534, L89 (2000)

Caffau, E., Ludwig, H.-G., Steffen, M., et al.: Astron. Astrophys. 488, 1031 (2008)

Caimmi, R.: Astron. Nachr. 318, 339 (1997)

Caimmi, R.: Astron. Nachr. 321, 323 (2000) (C00)

Caimmi, R.: Astron. Nachr. 322, 65 (2001a) (C00, erratum)

Caimmi, R.: Astron. Nachr. 322, 241 (2001b) (C01)

Caimmi, R.: New Astron. 12, 289 (2007) (C07)

Caimmi, R.: New Astron. 13, 314 (2008) (C08)

Carollo, D., Beers, T.C.Lee, Y.S., et al.: Nature 318, 1020 (2007)

Carretta, E., Gratton, R.G., Sneden, C.: Astron. Astrophys. 356, 238 (2000)

Centeno, R., Socas-Navarro, H.: Astrophys. J. Lett. 682, L61 (2008)

Chiba, M., Beers, T.C.: Astron. J. 119, 2843 (2000)

Fuhrmann, K.: Mon. Not. R. Astron. Soc. 384, 173 (2008)

Gratton, R.G., Carretta, E., Matteucci, F., Sneden, C.: Astron. Astrophys. 358, 671 (2000)

Gray, D.F.: The Observation and Analysis of Stellar Photospheres, Cambridge University Press, UK (2005)

Haywood, M.: Mon. Not. R. Astron. Soc. 325, 1365 (2001)

Haywood, M.: Mon. Not. R. Astron. Soc. 371, 1760 (2006)

Haywood, M.: Mon. Not. R. Astron. Soc. 388, 1175 (2008)

Henry, R.B.C., Worthey, G.: PASP 111, 919 (1999)

Holmberg, J., Nordström, B., Andersen, J.: Astron. Astrophys. 475, 519 (2007)

Horellou, C., Berge, J.: Mon. Not. R. Astron. Soc. 360, 1393 (2005)

Ibata, R.A., Gilmore, G.F.: Mon. Not. R. Astron. Soc. 275, 605 (1995)

Israelian, G., Rebolo, R., Garcia-Lopez, R.J., Bonifacio, P., Molaro, P., Basri, G., Shchukina, N.: Astrophys. J. 551, 833 (2001)

Ivezic, Z., Sesar, B., Juric, M., et al.: Astrophys. J. 684, 287 (2008)

Jørgensen, B.R., 2000. Astron. Astrophys. 363, 947.

Landi, E., Feldman, U., Doschek, G.A.: Astrophys. J. 659, 743 (2007)

Malinie, G., Hartmann, D.H., Clayton, D.D., Mathews, G.J.: Astrophys. J. 413, 633 (1993)

Melendez, J.: Astrophys. J. 615, 1042 (2004)

Melendez, J., Asplund, M., Alves-Brito, A., et al.: Astron. Astrophys. 484, L21 (2008)

Meusinger, H., Stecklum, B., Reimann, H.-G.: Astron. Astrophys. 245, 57 (1991)

Mota, D.F., van de Bruck, C.: Astron. Astrophys. 421, 71 (2004)

Nordström, B., Mayor, M., Andersen, J., et al.: Astron. Astrophys. 418, 989 (2004)

Norris, J.E.: Astrophys. J. Lett. 314, L39 (1987)

Pagel, B.E.J.: The G-dwarf Problem and Radio-active Cosmochronology. In: Beckman J.E., Pagel B.E.J. (eds.) Evolutionary Phenomena in Galaxies, Cambridge Univ. Press, p. 201 (1989)

Pagel, B.E.J., Patchett, B.E.: Mon. Not. R. Astron. Soc. 172, 13 (1975)

Prantzos, N.: Astron. Astrophys. 284, 477 (1994)

Prantzos, N.: EAS Publications Series, vol. 32, pp. 311-356 (2008)

Prantzos, N., Aubert, O.: Astron. Astrophys. 302, 69 (1995)

Prochaska, J.X., Naumov, S.O., Carney, B.W., McWilliam, A., Wolfe, A.M.: Astron. J. 120, 2513 (2000)

Ramirez, I., Allende Prieto, C., Lambert, D.L.: Astron. Astrophys. 465, 271 (2007)

Rocha-Pinto, H.J., Maciel, W.J.: Mon. Not. R. Astron. Soc. 279, 447 (1996)

Rocha-Pinto, H.J., Maciel, W.J., Scalo, J., Flynn, C.: Astron. Astrophys. 358, 850 (2000)

Roškar, R., Debattista, V.P., Quinn, T.R., et al.: Astrophys. J. Lett. 684, L79 (2008)

Ryan, S.G., Norris, J.E.: Astron. J. 101, 1865 (1991)

Ryden, B.S.: Astrophys. J. 329, 589 (1988)

Sadler, E.M., Rich, R.M., Terndrup, D.M.: Astron. J. 112, 171 (1996)

Schörck, T., Christlieb, N, Cohen, J.G., et al.: arXiv:0809.1172v1 (2008)

Schönrich, R., Binney, J.: Mon. Not. R. Astron. Soc. in press, (arXiv:0809.3006v1 [astro-ph], 2008) (2009)

Sellwood, J.A., Binney, J.: Mon. Not. R. Astron. Soc. 336, 785 (2002)

Smith, B.D., Tuck, M.J., Sigurdsson, S., et al.: Astrophys. J. 691, 441 (2009)

Socas-Navarro, H., Norton, A.A.: Astrophys. J. Lett. 660, L153 (2007)

Sofia, U.J., Meyer, P.M.: Astrophys. J. Lett. 554, L221 (2001)

Sommer-Larsen, J., Beers, T.C., Flynn, C., et al.: Astrophys. J. 481, 775 (1997)

Takada-Hidai, M., Takeda, Y., Sato, S., Sargent, W.L., Lu, L., Barlow, T., Jugeku, J.: New Astron. Rev. 45, 549 (2001)

Tinsley, B.M.: Fundam. Cosmic Phys. 5, 287 (1980)

Wang, B., Silk, J.: Astrophys. J. 406, 580 (1993)

Wielen, R. Astron. Astrophys. 60, 263 (1977)

Wielen, R., Fuchs, B., Dettbarn, C.: Astron. Astrophys. 314, 438 (1996)

Worthey, G., Dorman, B., Jones, L.A.: Astron. J. 112, 948 (1996)

Wyse, R.F.G., Gilmore, G.: Astron. J. 104, 144 (1992)

Wyse, R.F.G., Gilmore, G.: Astron. J. 110, 2771 (1995)

Zoccali, M., Hill, V., Lecureur, A., et al.: Astron. Astrophys. 486, 177 (2008)

Zurek, W.H., Quinn, P.J., Salmon, J.K.: Astrophys. J. 330, 519 (1988)

This manuscript was prepared with the AAS LaTeX macros v5.2.

Appendix

A Caption of symbols

To help the reader, the meaning of the parameters listed in the Tables throughout the paper, is explained below. The end of evolution is denoted by the index, f. For further details refer to parent papers (C00, C01, C07, C08).

Z_O Mass oxygen abundance.

ϕ Mass oxygen abundance normalized to the solar value.

$\Delta\phi$ Mass oxygen abundance (normalized to the solar value) bin, related to a selected [O/H] bin.

$\phi^{\mp}$ Upper (plus) and lower (minus) normalized oxygen abundance limit, related to an assigned normalized oxygen abundance bin, $\Delta\phi$.

$\Delta^{\mp}\phi$ Right (plus) and left (minus) normalized oxygen abundance interval semiamplitude related to an assigned normalized oxygen abundance bin, $\Delta\phi$.

$\Delta^*\phi'_\mathrm{R}$ Newly synthesised oxygen gas mass fraction (normalized to the solar value) within an active region, in inhomogeneous models of chemical evolution, at the end of a step.

$\Delta^*\phi$ Newly synthesised oxygen gas mass fraction (normalized to the solar value) within the whole system, in inhomogeneous models of chemical evolution, at the end of a step during the expected evolution.

ψ Empirical differential oxygen abundance distribution (EDOD).
Theoretical differential oxygen abundance distribution (TDOD).

$\psi^{\mp}$ Upper (plus) and lower (minus) EDOD limit related to an assigned normalized oxygen abundance bin, $\Delta\phi$.

$\Delta^{\mp}\psi$ Top (plus) and bottom (minus) EDOD interval semiamplitude related to an assigned normalized oxygen abundance bin, $\Delta\phi$.

ψ_0 Theoretical differential oxygen abundance distribution (exact value) at the starting point of the expected evolution (C01, C07).

$\psi_1(40)$ Theoretical differential oxygen abundance distribution (exact value) at the ending point of the first step of the expected evolution [C01, C07, Eq. (40)].

$\psi_1(41)$ Theoretical differential oxygen abundance distribution (second-order approximation) at the ending point of the first step of the evolution in the general case [C01, C07, Eq. (41)].

μ'_R Gas mass fraction which allows star formation within an active region at the end of a step.

D'_R Gas mass fraction which inhibits star formation within an active region at the end of a step. Negative values denote enhancement of star formation due to gas inflow.

s'_R Long-lived star mass fraction within an active region at the end of a step.

q Effective gas mass fraction within a region at the end of a step.

μ Gas mass fraction which allows star formation.

D Gas mass fraction which inhibits star formation. Negative values denote enhancement of star formation due to gas inflow.

s Long-lived star mass fraction.

α Mass fraction of a star generation which remains locked up in long-lived stars and stellar remnants.

κ Ratio of gas mass fraction which inhibits star formation to long-lived star and stellar remnant mass fraction. Negative values denote enhancement of star formation due to gas inflow.

m_mf Lower mass limit of long-lived stars.

$\hat{p}$ True oxygen yield.

$\hat{p}'$ Effective oxygen yield related to both inhomogeneous star formation and inhibited or enhanced star formation.

$\hat{p}''$ Effective oxygen yield related to inhibited or enhanced star formation.

χ Probability of a region being active.

B Table 8

Table 8 is exceedingly large in the text, and for this reason it is broken to be completely accessible.

Table 11 Table 8, left.

	DB12	DB13	DB14	DB15
$\mu'_{\rm R}$	1.3243 E−1	1.2295 E−1	1.1258 E−1	1.0304 E−1
q	6.1771 E−1	5.5533 E−1	4.9941 E−1	4.4924 E−1
χ	4.4156 E−1	5.0700 E−1	5.6410 E−1	6.1403 E−1
$\hat{p}/(Z_{\rm O})_\odot$	9.0478 E−1	8.3518 E−1	7.7553 E−1	7.2382 E−1
$\hat{p}'/(Z_{\rm O})_\odot$	3.6191 E−1	3.3407 E−1	3.1021 E−1	2.8953 E−1
μ_f	1.4559 E−1	9.5108 E−2	6.2204 E−2	4.0731 E−2
$\alpha_{2.9}$	6.9505 E−1	7.1175 E−1	7.2671 E−1	7.4020 E−1
$\alpha_{2.35}$	8.6951 E−1	8.7833 E−1	8.8803 E−1	8.9281 E−1
$(\widetilde{m}_{\rm mf})_{2.9}$	4.0227 E−1	3.7813 E−1	3.5660 E−1	3.3728 E−1
$(\widetilde{m}_{\rm mf})_{2.35}$	1.1305 E−2	9.3463 E−3	7.8194 E−3	6.6108 E−3
$\Delta^*\phi$	1.7435 E−1	1.9650 E−1	2.1539 E−1	2.3168 E−1
$\Delta^*\phi'_{\rm R}$	1.8170 E−0	1.7505 E−0	1.6938 E−0	1.6450 E−0
$-\psi_o$	2.4322 E−1	1.7337 E−1	1.1035 E−1	5.3384 E−2
$-\psi_1(40)$	2.8439 E−1	2.2346 E−1	1.6926 E−1	1.2104 E−1
$-\psi_1(41)$	2.8506 E−1	2.2446 E−1	1.7066 E−1	1.2289 E−1
κ	1.4286 E−1	2.3810 E−1	3.3333 E−1	4.2857 E−1
$s'_{\rm R}$	7.5755 E−1	7.0839 E−1	6.6557 E−1	6.2787 E−1
$D'_{\rm R}$	1.0822 E−1	1.6866 E−1	2.2186 E−1	2.6909 E−1
$\overline{\phi}$	7.8307 E−1	7.4978 E−1	7.2065 E−1	6.9485 E−1
s_f	7.4761 E−1	7.3087 E−1	7.0335 E−1	6.7149 E−1
D_f	1.0680 E−1	1.7402 E−1	2.3445 E−1	2.8778 E−1

Table 12 Table 8, right.

	DN	DN4	DN5	DN6	DN7
$\mu'_{\rm R}$	1.6663 E−1	3.7477 E−1	3.6662 E−1	3.5864 E−1	3.5083 E−1
q	8.0550 E−1	9.6146 E−1	9.3741 E−1	9.1396 E−1	8.9109 E−1
χ	2.3339 E−1	6.1635 E−2	9.8821 E−2	1.3416 E−1	1.6776 E−1
$\hat{p}/(Z_{\rm O})_\odot$	7.2382 E−1	1.8096 E−0	1.4476 E−0	1.2064 E−0	1.0340 E−0
$\hat{p}'/(Z_{\rm O})_\odot$	2.8953 E−1	1.0857 E−0	8.6859 E−1	7.2382 E−1	6.2042 E−1
μ_f	4.4842 E−3	3.7439 E−1	1.9872 E−1	1.0548 E−1	5.5988 E−2
$\alpha_{2.9}$	7.4020 E−1	5.3263 E−1	5.8755 E−1	6.3092 E−1	6.6604 E−1
$\alpha_{2.35}$	8.9281 E−1	7.6914 E−1	8.0638 E−1	8.3327 E−1	8.5360 E−1
$(\widetilde{m}_{\rm mf})_{2.9}$	3.3728 E−1	6.4228 E−1	5.6022 E−1	4.9602 E−1	4.4449 E−1
$(\widetilde{m}_{\rm mf})_{2.35}$	6.6108 E−3	5.1835 E−2	3.2618 E−2	2.1898 E−2	1.5436 E−2
$\Delta^*\phi$	6.2622 E−2	4.2667 E−2	5.6142 E−2	6.5123 E−2	7.1537 E−2
$\Delta^*\phi'_{\rm R}$	1.2971 E−0	1.7760 E−0	1.4526 E−0	1.2370 E−0	1.0831 E−0
$-\psi_o$	4.8961 E−2	1.2641 E−0	1.0696 E−0	9.0546 E−1	7.6482 E−1
$-\psi_1(40)$	5.0826 E−1	1.2692 E−0	1.0780 E−0	9.1713 E−1	7.7976 E−1
$-\psi_1(41)$	5.0839 E−1	1.2692 E−0	1.0780 E−0	9.1718 E−1	7.7985 E−1
κ	4.2857 E−1	−4.2857 E−1	−2.8571 E−1	−1.4286 E−1	0.0000 E−0
$s'_{\rm R}$	5.8336 E−1	1.0942 E−0	8.8673 E−1	7.4825 E−1	6.4917 E−1
$D'_{\rm R}$	2.5001 E−1	−4.6892 E−1	−2.5335 E−1	−1.0689 E−1	0.0000 E−0
$\overline{\phi}$	8.6448 E−1	1.1450 E−0	1.0068 E−0	9.1462 E−1	8.4870 E−1
s_f	6.9686 E−1	1.0948 E−0	1.1218 E−0	1.0436 E−0	9.4401 E−1
D_f	2.9865 E−1	−4.6921 E−1	−3.2051 E−1	−1.4909 E−1	0.0000 E−0